Stability of a numerical scheme for methane transport in hydrate zone under equilibrium and non-equilibrium conditions

Malgorzata Peszynska and Choah Shin

ABSTRACT. In this paper we carry out numerical analysis for a family of simplified gas transport models with hydrate formation and dissociation in subsurface, in equilibrium and non-equilibrium conditions. These models are adequate for simulation of hydrate phase change at basin and at shorter time scales, but the analysis does not account directly for the related effects of evolving hydraulic properties.

To our knowledge this is the first analysis of such a model. It is carried out for the transport steps while keeping the pressure solution fixed. We frame the transport model as conservation law with a non-smooth space-dependent flux function; the kinetic model approximates this equilibrium. We prove weak stability of the upwind scheme applied to the regularized conservation law. We illustrate the model, confirm convergence with numerical simulations, and illustrate its use for some relevant equilibrium and non-equilibrium scenarios.

Keywords: Methane hydrate and transport and numerical analysis and stability and conservation law and kinetic and equilibrium model

1. Introduction

In this paper we analyze a computational model for transport of methane in hydrate zone at the equilibrium and kinetic time scales. Our interest in methane hydrate comes from collaborations with geophysicists who aim to explain and predict hydrate deposits found in nature. The simulations of hydrate evolution have been carried out by many researchers including in [10, 11, 34, 35, 36, 39, 44, 49, 50, 71, 70]; however, our paper appears to be the first one to analyze the numerical schemes.

Methane hydrate, also known as "Ice That Burns" is an ice-like crystalline substance made of methane molecules enclosed in a cage made by water molecules. Methane hydrate is abundant in deep sub-sea sediments whenever favorable conditions of high pressure, low temperature, and large supply of methane hold. Methane hydrate is also found in the Arctic below permafrost.

To explain the presence and shape of hydrate deposits found in nature, as well as to understand the methane fluxes as a response to the climate change, various simulations were carried out; see, e.g., [15, 20, 35, 49, 50, 62, 65, 70, 71]. These simulations are typically carried out at the *basin time scales* of several kilo-years or at least years or months. The presence of hydrate is explained with a postulate of supply of gas from deep Earth sources or

Department of Mathematics, Oregon State University, Corvallis, OR 97330

E-mail address: (M. Peszynska) mpesz@oregonstate.edu, (C. Shin) shinc@oregonstate.edu.

Date: Article accepted for publication by the Journal of Computational Geosciences on March 16, 2021.

This research was partially supported by NSF DMS-1522734 "Phase transitions in porous media across multiple scales" and DMS-1912938 "Modeling with Constraints and Phase Transitions in Porous Media", NSF IRD plan 2019-20, and Martin-O'Neill COS Fellowship.

by existence of biogenic sources of methane such as microbial species; see [35, 49, 62]. Recent studies focus also on the dissociation of hydrate deposits in response to the environmental conditions such as an increase in average 9 temperatures and address the impact of hydrate on the balance of greenhouse gases [4, 10, 13, 22, 58] at the time scale of years or decades.

Hydrate has also been evaluated as a potential energy source [1, 42, 54]. In particular, in the pilot projects in Japan and Alaska [2, 42, 60], the recovery of methane is enabled by lowering the pressure in the wells which triggers hydrate dissociation and release of large amounts of gas. A similar mechanism contributes to hazard while drilling [8, 19, 57], with the characteristic time scale of days.

Overview: In this paper we analyze a discrete model of hydrate formation and dissociation which describes methane transport by advection and diffusion coupled to phase behavior in equilibrium and non-equilibrium conditions and two-phase liquid-hydrate conditions, and which treats phase behavior in a sequential way with macro-time steps. The equilibrium model is a simplified version of the comprehensive model [35] presented earlier in [49, 50]. Kinetic models from the literature [14, 17, 18, 26, 65] are formulated for the general context of three-phase equilibria; our model resembles these but covers both unsaturated as well as saturated conditions in liquid-hydrate conditions. The scheme combines finite volume spatial discretization with implicit-explicit time discretization, and uses the formal mathematical framework of multivalued graphs. This framework for the equilibrium model is equivalent to variable switching as we demonstrated in [16]. Our analysis of the kinetic model with this framework supports the understanding of the equilibrium as the limit of kinetic model under fast reaction rates.

Our main contribution is the analysis of numerical stability of the advective model in equilibrium and non-equilibrium, as well as demonstration of the convergence of the scheme at the rate $O(\sqrt{h})$ common for generic scalar conservation laws. The analysis applies to the transport in liquid-hydrate zone under various simplifying assumptions including long time range, close to geothermal temperature distribution, close to hydrostatic pressure distribution, modest gas supply, and constant salinity. We make a-priori assumptions on the data and illustrate the sensitivity of the model to data as guided by the analysis. In particular, our analyses explain the feature of discontinuous hydrate lenses observed in nature and exacerbated in heterogeneous sediments. The scheme for the kinetic model is shown to be robust across the saturated and unsaturated conditions.

To our knowledge, our analysis is the first of this kind for advective transport in either the equilibrium and kinetic setting for hydrate models. Our analysis applies only to the simplified model with which we simulate hydrate phase change, but does not directly apply to the possibly strongly coupled effects like evolving hydraulic properties which are critical for simulation of hydrate evolution and recycling. Our results are therefore the first step towards future work on the analysis of schemes for more comprehensive models. The paper also includes auxiliary supporting results which can be used in a more general context.

Plan of the paper: We start with auxiliary notation on evolution with multivalued monotone graphs in Sec. 2. In Sec. 3 we provide details of the transport model, starting with the equilibria, and in Sec. 4 we describe the kinetic models. In Sec. 5 we define the numerical schemes. In Sec. 6 we analyze the numerical scheme for the equilibrium model and in Sec. 7 we analyze the scheme for the kinetic model. Finally, in Sec. 8 we present numerical results: we present convergence studies in the case covered by the theory as well as simulation

results in realistic examples including the comparison of equilibrium and kinetic models. We conclude in Sec. 9. The Appendix in Sec. 10 provides extensive auxiliary results.

2. Notation and background for ODEs with monotone graphs.

We recall here the notation and a few elements of the mathematical framework of evolution equations with monotone multivalued graphs on \mathbb{R} to extend what is known for the initial value problem $\frac{da}{dt} + G(a) = f, a(0) = a^0$ when $G : \mathbb{R} \to \mathbb{R}$ is a monotone increasing function. These extensions are useful for modeling phase equilibria and kinetic schemes. We refer to the comprehensive details on the general abstract Hilbert space setting and monotone multivalued operators provided, e.g., in [5, 56]. We need the notation and basic properties in our estimates and analyses.

We recall that for a relation (graph) $G \subset \mathbb{R} \times \mathbb{R}$, its domain $(G) = \{a : \exists b : (a, b) \in G\} \subset \mathbb{R}$, and the inverse $G^{-1} = \{(b, a) : (a, b) \in G\}$. The graph G is monotone if $\forall (a_1, b_1), (a_2, b_2) \in G$ we have $(b_2 - b_1)(a_2 - a_1) \geq 0$. If $(a, b) \in G$, and G is monotone multivalued, we will write $b \in G(a)$ to denote some selection b out of the set G(a). This selection is not unique, hence the symbol " \in ". Further, G is maximal monotone if I + G is onto \mathbb{R} . For a maximal monotone G and A > 0, the resolvent

$$\mathcal{R}_{\lambda}^{G} = (I + \lambda G)^{-1} \tag{1}$$

is a contractive function, and the solution to $a+\lambda G(a)\ni f$ is unique and given by $a=\mathcal{R}_{\lambda}^G(f)$. **Evolution ODE with graph:** The resolvent \mathcal{R}_{λ}^G helps to define the solution to an evolution problem

$$\frac{da}{dt} + G(a) \ni f; \quad a(0) = a^0, \tag{2}$$

where $f \in L^1(0,T)$ is some given input and where $a^0 \in \text{domain}(G) \subset \mathbb{R}$ is some initial data. The C^0 solution a(t) to (2) is defined as the limit as $\tau \to 0$ of the fully implicit finite difference step function solutions $a^n \approx a(t^n)$, with $t^n = n\tau$, to the inclusion

$$\frac{a^n - a^{n-1}}{\tau} + G(a^n) \ni f^n, \ n \ge 1.$$
 (3)

In spite of the symbol \in , the step solution $a^n \in \text{domain}(G)$ to (3) is uniquely defined $a^n = \mathcal{R}_{\tau}^G(a^{n-1} + \tau f^n)$. Once we know a^n , the actual selection $G(a^n) = f^n - \frac{a^n - a^{n-1}}{\tau}$ is given uniquely from (3).

In this paper we use various single-valued approximations $G_{\lambda} \approx G$ which are maximal monotone when G is. One is the Yosida approximation $G_{\lambda} = \frac{1}{\lambda}(I - \mathcal{R}_{\lambda}^{G})$ which provides another way to define the solution a(t) to (2) as the limit as $\lambda \to 0$ of $a_{\lambda}(t)$, the family of solutions to the ODE $\frac{da_{\lambda}}{dt} + G_{\lambda}(a_{\lambda}) = f$.

Evolution system with graphs: In addition to (2), we consider the following system on $\mathbb{R} \times \mathbb{R}$

$$\frac{d}{dt}a = Q, \frac{d}{dt}b = -Q; \ a(0) = a^0, b(0) = b^0.$$
 (4)

We are interested in the case when $Q(a,b) \in b - G(a)$ is multivalued with $G(\cdot)$ is monotone. Here the first and the second equations have similar properties to (2) but are coupled. Adding the two equations leads to $a(t) + b(t) = \text{const} = a^0 + b^0$. With the abstract theory from [56], it is easy to show that the system (4) is well-posed in $\mathbb{R} \times \mathbb{R}$. We also see that the solutions

(a(t),b(t)) evolve towards some (a^{∞},b^{∞}) which is at the intersection of G with the manifold $a+b=a^0+b^0$.

Special graphs used in this paper: The graph $\operatorname{sgn}(x)$ assigns -1 to x < 0, 1 to x > 0, and the set [-1,1] to x = 0, and we write $\operatorname{sgn}(x) = (-\infty,0) \times \{-1\} \cup \{0\} \times [-1,1] \cup (0,\infty) \times \{1\}$. This graph $\operatorname{sgn}(x)$ is distinct from the single valued discontinuous function $\operatorname{sgn}_0(x)$ which agrees with $\operatorname{sgn}(x)$ for $x \neq 0$ but assigns 0 to x = 0. The Heaviside graph $H(x) = \frac{1}{2}(1 + \operatorname{sgn}(x))$ assigns 0 to x < 0, 1 to x > 0, and the set [0,1] to x = 0. We also use $x_+ = \max(0, x)$.

3. Transport Model under Equilibrium and Kinetic Phase Constraints

Methane is present in sub-ocean sediments and Arctic regions due to biogenic sources and from upward fluxes from the deeper Earth layers [35]. It is transported by diffusion and advective fluxes, and can be present in liquid, gas or solid phases. The partition of methane component between phases depends on the pressure and temperature and on the amount of methane component. With small amounts of methane and at large depths (i.e., large pressures), methane is dissolved in the aqueous (liquid) brine phase denoted by l. With larger amounts of methane and at low temperatures, the solid phase made of methane and water in fixed proportions precipitates; this solid phase denoted by h is called methane hydrate (clathrate or methane ice). At higher temperatures, the hydrate phase is not stable and free gas phase forms. A typical distribution of phases in sub-ocean sediments is that the solid hydrate phase is stable and present at low temperatures; specifically, this occurs above the so-called Bottom Hydrate Stability Zone (BHSZ). In turn, below BHSZ, only the gas phase is stable. Phase equilibria represent the tendency of a system to maintain low energy, and correspond to the most stable distribution of components between phases.

The phase distributions may not always follow equilibria; this is common at short time scales, e.g., after seismic events which alter the distribution of gases and sediments, or during production of gas from subsurface. Our work in this paper addresses equilibrium models as well as certain selected scenario of non-equilibria. In this paper we do not account for the presence of free gas such as ex-solved gas or from buoyant gas travelling upwards. The analysis of a model involving gas is the subject of current work.

In this section we describe a model accounting for methane transport above BHSZ in a porous reservoir $\Omega \subset \mathbb{R}^d$, over time t, either under the assumption of phase equilibria or allowing non-equilibria. For phase equilibria we follow closely the comprehensive model in [35] in the hydrate zone which we simplified in [49, 50] for the purposes of efficient simulations; we used real reservoir data and experimental observations to motivated the reduced model; see also our well-posedness analysis of the reduced model in [16, 48].

Our objectives in this paper are to (i) provide an analysis of the finite volume discretization of the reduced equilibrium model from [49, 50], which we accomplish for a regularization of the original model. Our analysis also (ii) explains the shape of hydrate deposits observed in nature as well as the hydrate saturation profiles found in computational simulations. Our main result is (iii) the study of a new non-equilibrium model for hydrate in under-saturated and over-saturated conditions above BHSZ which extends literature, and for which we are able to prove rigorous numerical stability.

Below we briefly recall the equilibrium model from [48]; it is the same as that in [49, 50] under the assumption of constant salinity. We also motivate and explain the non-equilibrium models which we compare to other kinetic models in the literature.

- 3.1. **Assumptions.** We make the following assumptions in the model development.
- (A1) The reservoir Ω is in the hydrate stability zone, i.e., only the liquid and hydrate phases are stable.
- (A2) Free gas is not present in Ω , i.e., there is abundant water present for hydrate formation; see [35]

In addition, the following assumptions are made for the sake of presentation and analysis, but are not needed for the computational model or for simulations.

- (A3) Liquid and hydrate phases are incompressible.
- (A4) The sediment is rigid, and the porosity $\phi(x,t) \approx \phi(x)$ is fixed.
- (A5) Salinity $\chi_{lS}(x,t) = \chi_{lS}^{sw} = \text{const equals seawater salinity } \chi_{lS}^{sw}$.
- 3.2. Mass conservation equations. Consider (x,t) at a point $x \in \Omega$ and time t > 0. We denote the mass fraction of methane in the liquid phase by $\chi(x,t)$ and the volume fraction of hydrate by S(x,t). With (A1) and (A2), the total mass density of methane at (x,t) is $\rho_l u = (1-S)\rho_l \chi + S\rho_h \chi_{Mh}$ with ρ_l, ρ_h denoting mass density of brine and of hydrate, respectively, and χ_{Mh} denoting the mass fraction of methane in the hydrate phase, which is a known fixed constant. The mass conservation equation for methane component in porous sediment of porosity ϕ is thus

$$\partial_t \left(\phi \rho_l u \right) + \nabla \cdot \left(q \rho_l \chi \right) - \nabla \cdot \left(\rho_l d_m \nabla \chi \right) = F_M. \tag{5a}$$

Here d_m is diffusivity and q is the Darcy flux defined below. Also, F_M accounts for methane sources, e.g., biogenic production of methane by microbes, or sink terms relevant for the production scenarios. We also rewrite

$$u = (1 - S)\chi + RS = \chi + S(R - \chi).$$
 (5b)

Here $R=\frac{\rho_h\chi_{Mh}}{\rho_l}\approx\chi_{Mh}$ since $\rho_h\approx\rho_l$. In practice, with the values reported in [49]; $R=0.1203~{\rm kg/kg}$, we have $\rho_l=1030~{\rm kg/}m^3$, $\rho_h=925~{\rm kg/}m^3$, while ${\rm max}_x\,\chi^*(x)\approx 2.4\times 10^{-3}~{\rm kg/kg}$ for the case of UBGH2-7 as given in [49]. From now on we will assume

$$0 < \chi^* < R. \tag{6}$$

With the single equation (5) involving two variables u and S or χ and S, we close the system by either assuming equilibrium conditions binding χ and S, or setting up a non-equilibrium model which evolves towards the equilibrium. We describe the equilibrium model in Sec. 3.4 and the non-equilibrium models in Sec. 4.

The model (5) is complemented with the mass conservation equation for water component whose concentration is $1 - \chi$ in liquid phase and $1 - \chi_{Mh}$ in the hydrate phase. The model for water mass conservation is

$$\partial_t \left(\phi \left[(1 - S)\rho_l (1 - \chi) + S\rho_h (1 - \chi_{Mh}) \right] \right) + \nabla \cdot (q\rho_l (1 - \chi)) = 0.$$
 (7)

3.3. **Pressure equation.** The pressure equation follows by adding (5a) with (5b) and (7); with Darcy's law we obtain

$$\partial_t \left(\phi \left[(1 - S)\rho_l + S\rho_h \right] \right) + \nabla \cdot (q\rho_l) - \nabla \cdot (\rho_l d_m \nabla \chi) = F_M, \tag{8a}$$

$$q = -\frac{K}{\mu_l} (\nabla P - \rho_l G \nabla d), \tag{8b}$$

with Darcy flux q, pressure P(x,t), permeability K, liquid phase viscosity μ_l , and depth d(x). Here K = K(x; S) depends on the presence of hydrate in the pore-space, with empirical data, e.g., in [35]. Typically $K(\cdot; S)$ decreases with S, and the porous matrix is plugged up when hydrate saturation is close to 1.

At large time scales such as in basin modeling the pressure follows distribution close to hydrostatic with q = 0. Otherwise there can be gas fluxes with $q \neq 0$, e.g., from deep in the Earth's crust upwards, and we must solve (8) under given boundary conditions. One practical scenario is when q is given at the bottom of the reservoir, and a fixed pressure is known at the top, e.g., from the known height of water column. Rewriting (8) as

$$\nabla \cdot q = \frac{F_M}{\rho_l} + \nabla \cdot (d_m \nabla \chi) + \partial_t \left(\phi S \frac{\Delta \rho}{\rho_l} \right), \quad \Delta \rho = \rho_l - \rho_h, \tag{9}$$

allows to study contributions to local variations of q. We see that the magnitude of the first and second terms on the right hand side is modest in realistic settings [49]. However, the third term may contributes to the local increase of velocity due to the density difference $\Delta \rho$ whenever $S \uparrow$ increases rapidly.

3.4. Phase equilibria for hydrate crystal formation. The formation of a hydrate crystal out of liquid phase usually involves the processes of nucleation, diffusion of molecules towards the existing cages, and the adsorption of new crystals, see, e.g., molecular dynamics simulations in [57, 66] at time scales of 10^{-6} [s]. At the reservoir time scales of transport the hydrate formation or dissociation is modeled by an aggregate of the microscopic processes; one assumes either an equilibrium presented here or a kinetic model discussed in Sec. 4.

In equilibrium, the hydrate forms only if the methane concentration χ in water has reached its maximum solubility denoted by χ^* . When the hydrate crystals form, we have that S>0 and $\chi=\chi^*$, the saturated case. When $\chi<\chi^*$, no hydrate exists, and S=0. This is expressed by the constraint

$$\begin{cases} \chi \le \chi^*, & S = 0, \\ \chi = \chi^*, & S > 0. \end{cases}$$
 (10)

Next we write an explicit formula for the dependence of the total amount of methane u on (χ, S) . At a given (x, t) with $\chi^*(x, t)$ known, we have

$$u = \begin{cases} \chi, & u \le \chi^*, S = 0, \\ (1 - S)\chi^* + SR, & u \ge \chi^*, S \ge 0. \end{cases}$$
 (11)

Conversely, given u, the equilibrium values χ and S on E_* are given uniquely

$$\chi = \min\{\chi^*, u\} \quad \text{and} \quad S = \frac{(u - \chi^*)_+}{R - \chi^*}.$$
(12)

The relationship (12) can be used at any (x,t) to get the unique values $\chi(x,t)$ and S(x,t) from u(x,t). The quantity $\chi^* = \chi^*(P,T,\chi_{lS})$ depends on the pressure P and temperature T,

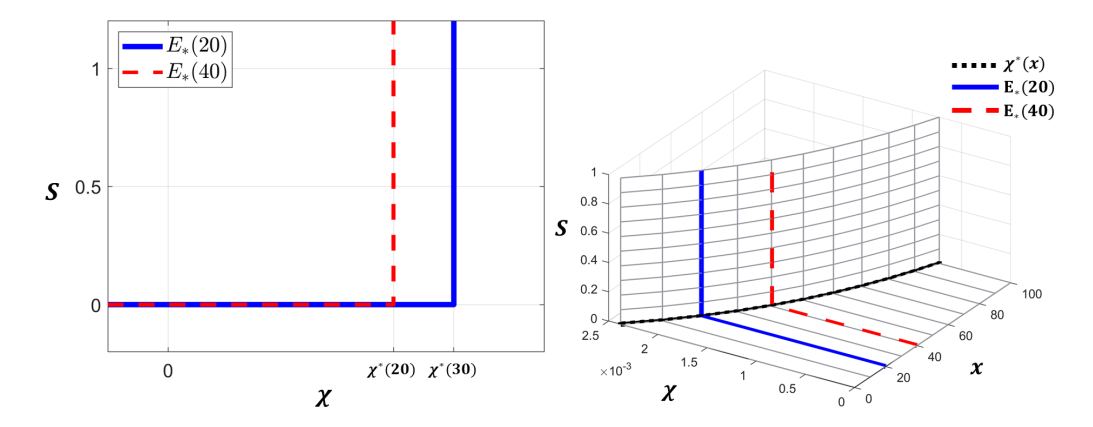


FIGURE 1. Illustration of graph E_* with data from Ulleung Basin case UBGH2-7 [49], where $\chi^*(x) \approx 0.0024e^{-0.012x}$. Left: the portion of $E_* = E_*(x)$ for a fixed x. Right: multivariate view of $(\chi, S) \in E_*(x)$.

and salinity χ_{lS} . This dependence is resolved sequentially in our computational model: over some macro time step P, T are kept constant and χ^* depends on x only. This is discussed in detail later in Sec. 5.2.

3.4.1. Equilibrium model with multivalued graphs. The formulas (10)–(12) are simple and explicit. For the needs of the kinetic model to be defined, we note that the variables (χ, S) "live" on the graph $E_* = E_*^- \cup E_*^+$ defined as

$$(\chi, S) \in E_* = (-\infty, \chi^*] \times \{0\} \cup \{\chi^*\} \times [0, \infty),$$
 (13)

with $E_*^- = (-\infty, \chi^*] \times \{0\}$, $E_*^+ = \{\chi^*\} \times [0, \infty)$, as illustrated in Fig. 1. The inverse graph $W_* = E_*^{-1}$ is

$$W_*(S)\ni\chi\equiv(S,\chi)\in W_*=\{0\}\times(-\infty,\chi^*]\cup[0,\infty)\times\{\chi^*\}.$$

It is easy to see that both E_* and W_* are maximal monotone. In what follows we write $S \in E_*(\chi)$ or $\chi \in W_*(S)$. These graphs are set-valued, but in evolution models, the particular selection out of these graphs is actually unique, as discussed in Sec. 2.

Remark 1. Not all the points on the graph E_* (13) are physically meaningful. In particular, any reasonable calculated values of concentrations and saturations should satisfy $\chi \geq 0$ and $0 \leq S < 1$. We denote by $E_*^0 = \{(\chi, S) \in E_* : \chi \geq 0; S < 1\}$ the physically meaningful portion of E_* . In addition, from (6) and (11) we see that if $(\chi, S) \in E_*^0$, then u satisfies

$$0 \le u(\chi, S) < R. \tag{14}$$

Conversely, for any u which satisfies (14), we have from (6) that (χ, S) given by (12) satisfies $0 \le \chi \le \chi^*$ and $0 \le S < 1$.

4. Transport model with Kinetic Phase Constraints

Kinetic models are common in geochemistry and chemical engineering [30, 75] and describe the evolution of a system towards thermodynamic equilibrium from some initial conditions out of equilibrium, e.g., in the processes of adsorption, phase transitions, and crystal precipitation and dissolution. The time scale of hydrate formation or dissociation is on the order of hours or days O([h]) - O([days]) [57, 73]. In production scenarios [23, 33, 42, 43, 72] this time scale is comparable to that of the transport processes. Comprehensive subsurface transport simulators including STOMP, TOUGH, PFLOTRAN, GEOS, Geo-COUS implement the complex kinetic exchange model in the applications using depressurization or thermal stimulation to aid methane recovery from hydrate; see e.g., the recent international code comparison studies [68, 69] led by DOE/NETL.

For modeling methane in the environment at large spatial scales, e.g., methane flux response to environmental temperature variations or abrupt geological events, some authors use kinetic models [6, 17, 18, 62, 65]. Finally, some computational models use kinetics rather than equilibria to implement or to approximate phase behavior regardless of the time scale considered [10, 53, 62].

A general kinetic model must predict the evolution of all relevant variables towards an equilibrium from some out-of equilibrium state, and is complemented by other equations which describe the evolution of all of (T, P, χ, S) towards some equilibrium $(T^{\infty}, P^{\infty}, \chi^{\infty}, S^{\infty})$, starting from some initial $(T^{0}, P^{0}, \chi^{0}, S^{0})$. The kinetics is coupled to the transport and constitutive equations, and would account for the presence of gas phase and capillary effects.

In the framework of our reduced model for liquid-hydrate zone we assume (P,T) are fixed over some time interval (t^{old}, t^{new}) with $t^{new} = t^{old} + \Delta t$. In equilibrium the variables $(\chi(x,t), S(x,t)) \in E_*(x)$ at every t. If the (P,T) conditions change at t^{new} , and a new $\chi^*_{new} = \chi^*(x, t^{new})$ is given, the variables (χ, S) are out of the equilibrium with respect to the new graph E^{new}_* . If Δt is really large we can assume they immediately adjust to the new equilibrium. Otherwise we need a kinetic model to describe the evolution of (χ, S) towards E^{new}_* .

Below we discuss kinetic models for hydrate, starting with literature review and a homogeneous "batch reactor" model, which we couple later with a transport model.

4.1. Kinetic models of hydrate formation: literature background. Following [7, 14, 17, 18, 26, 74], the kinetics of gas-liquid-hydrate phase system involves an exchange term Q proportional to the driving force in the three phase conditions,

$$\frac{d}{dt}S = Q = k(f_g - f_{eq}),\tag{15}$$

where k>0 is the hydrate formation or the dissociation rate, and where f_g , f_{eq} are the local gas fugacity, and the equilibrium fugacity at the given pressure and temperature, respectively. This expression (15) predicts that the hydrate forms when $f_g > f_{eq}$, and dissociates when $f_g < f_{eq}$. In [17, 18] the authors propose $Q \propto (P - P_{eq})$, with P_{eq} equal the equilibrium pressure for a given fixed T, and this approach models a response to the increase or decrease in pressure. A physically grounded expression for k is complex [61]. The rate $k \propto A_s$, the surface area available for the reaction to occur which is proportional to the effective porosity $\phi(1-S)$. In a three phase system the hydrate formation rate k also depends on the availability of water and methane (thus on the gas and aqueous phase saturations S_g and S_w); but for hydrate dissociation the rate k depends on availability of hydrate (thus on $S=1-S_g-S_w$). Therefore (15) is in general hysteretic; see also [73]. From mathematical point of view the presence of S or (1-S) in k keeps the variable S in physically meaningful domain $S \in [0,1]$. Model (15) is designed to work in the saturated case when $S^{\infty} > 0$, and $\chi^{\infty} = \chi^*$.

Our focus in this paper is on liquid-hydrate systems. For these, according to [6, 10], the driving force $f_g - f_{eq}$ in (15) can be expressed by the difference of methane concentration at the liquid-gas equilibrium and maximum methane solubility χ^* at three-phase equilibrium state for the given P and T. With no free gas, Q becomes

$$Q = k(\chi - \chi^*),\tag{16}$$

similar to that for crystal formation from saturated or oversaturated mixtures in geochemistry [75, 30]. In this paper we extend (16) so it can work well across the two-phase saturated as well as in single phase unsaturated conditions when $S^{\infty} = 0$, and $\chi^{\infty} < \chi^*$. We explain this extension in Sec. 4.2 with further details given in Sec. 10.2. Our model is robust, also when coupled to the transport model. In the future we hope to extend it to the three phase equilibria extending (15).

4.2. Kinetic batch reactor model model for hydrate evolution in liquid-hydrate conditions. Consider an isolated system, with P, T fixed and a fixed amount $u(\chi, S) = u^0$ of methane, and ignore any transport contributions or sources to focus on the distribution of methane between liquid and hydrate phases. The values $(\chi(t), S(t))$ live on a fixed curve

$$u(\chi, S) = \chi(1 - S) + RS = u^{0} = u(\chi^{0}, S^{0}), \tag{17}$$

in the (χ, S) plane. With some given χ^* , and a corresponding fixed multi-valued graph E_* , for a given u^0 , the equilibrium point lies at the intersection of the curve (17) with the graph E_* , and can be found from (12). The graph E_* and the curves (17) are illustrated in Fig. 2, with point (A) corresponding to an equilibrium case.

The case out of equilibrium (points (B) and (C) in Fig. 2) is when the pair (χ, S) on (17) is away from E_* . For example we can have $\chi(t) > \chi^*$ (B), or S(t) > 0 with $\chi(t) < \chi^*$ (C). As $t \uparrow \infty$, the points $(\chi(t), S(t))$ evolve from some (χ^0, S^0) towards some (χ^∞, S^∞) on E_* along the curve (17) according to some kinetic model with exchange rate Q.

We postulate now some conditions on (χ^0, S^0) and u^0 to guarantee that the kinetics leads to physically meaningful $(\chi^{\infty}, S^{\infty})$ on E_* . In particular, from Remark 1 we see that $u^{\infty} = u(\chi^{\infty}, S^{\infty})$ should satisfy $0 \le u^{\infty} < R$, thus we must have $0 \le u^0 = u(\chi^0, S^0) < R$. Also, non-negativity must be imposed on (χ, S) . In summary, we consider the physically meaningful region $(\chi, S) \in D^0 = [0, R) \times [0, 1)$.

Next, we aim to predict whether a given $u^0 = u(\chi^0, S^0)$ leads to $(\chi^{\infty}, S^{\infty}) \in E_*^-$ or to $(\chi^{\infty}, S^{\infty}) \in E_*^+$. In the latter saturated case we have $\chi^{\infty} = \chi^*$ and $S^{\infty} \in [0, 1)$, and $u^0 = u^{\infty} = \chi^{\infty} + (R - \chi^{\infty})S^{\infty} \ge \chi^*$ by (6). In the former case we have $u^0 \le \chi^*$. It is thus convenient to decompose $D^0 = D_-^0 \cup D_+^0$ as follows

$$D^{0}_{+} = \{(\chi, S) \in D^{0} : u(\chi, S) \ge \chi^{*}\};$$

$$D^{0}_{-} = \{(\chi, S) \in D^{0} : u(\chi, S) \le \chi^{*}\}.$$

Fig. 2 provides illustration of these definitions, and motivates our subsequent analyses.

4.2.1. Three batch kinetic models. Our objective is to construct a model which works well in all of D^0 . We start with (16) dubbed (KIN1) which works in D_+^0 . We include S in k_2 in a simpler model (KIN2) which works well also in D_+^0 only. Finally to allow the evolution towards a possible equilibrium on E_*^- or on E_*^+ we combine these two possible equilibria in (KIN3) using an abstract setting with the graph E_* . Each (KINj) has some rate k_j . In D_+^0

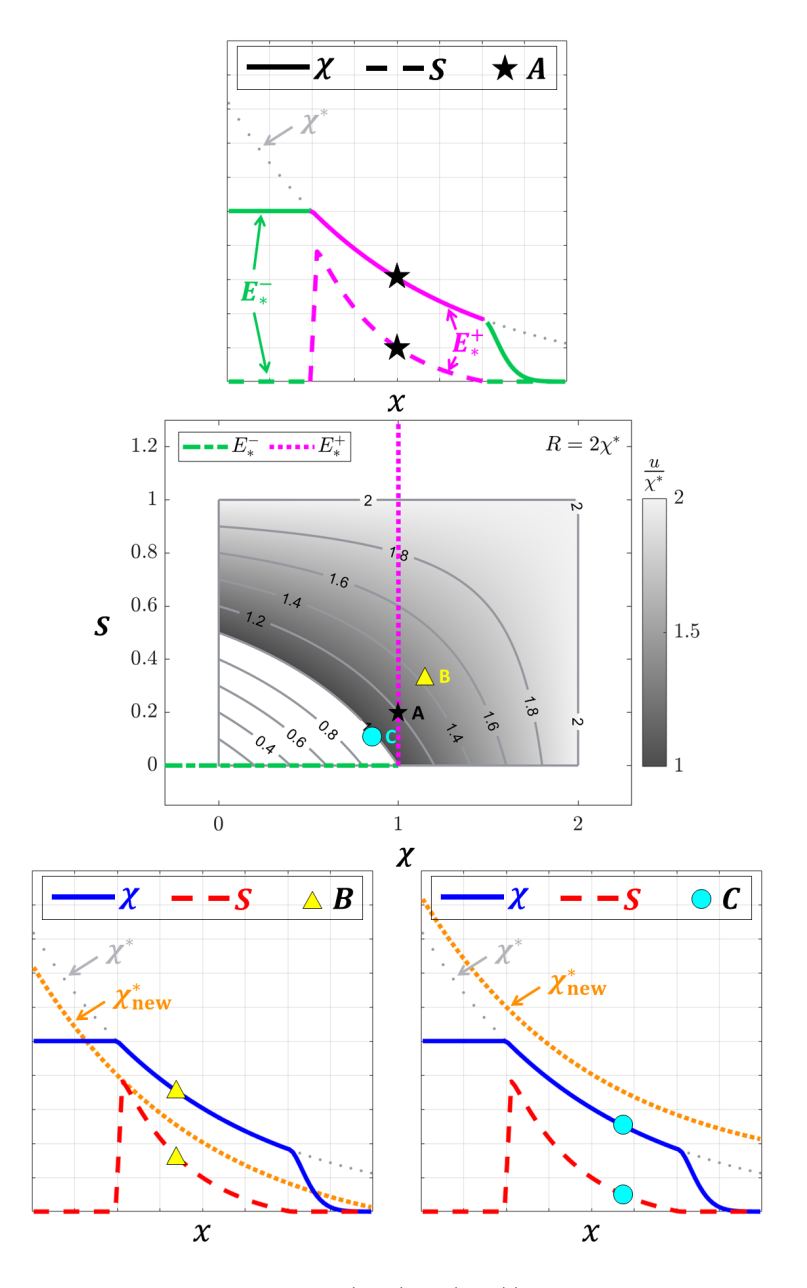


FIGURE 2. Illustration of typical $\chi(x,t), S(x,t)$ at some t in hydrate reservoir (top) $x \in \Omega$. For this illustration we choose $R = 2\chi^*$. Top: plot of χ, S) in equilibrium, with $\chi(x,t) \leq \chi^*(x), S(x,t) \geq 0$ and $(\chi(x,t), S(x,t)) \in E_*(x)$ as in (10). Middle: illustration of the graph $(\chi,S) \in E_*$ at the point A (equilibrium), and at the points B and C out of equilibrium (not on E_*) but within the physically meaningful region $(\chi,S) \in D^0 = [0,R) \times [0,1]$. The contours $u(\chi,S) = u^0$ of (17) in D^0 for $\frac{u^0}{\chi^*}$ equal 0.4, 0.6, ..., 1.8, with the curve $u(\chi,S) = u^0 = \chi^*$ separating the "saturated" region D_+^0 shaded in gray from the "un-saturated" region D_-^0 which is in white. The parts E_*^+ and E_*^- of E_* are in green and magenta. Bottom: an example of $\chi^*(x), \chi(x), S(x)$ in a reservoir in out of equilibrium conditions when (B) $\chi^*_{new} < \chi^*$, and (C) when $\chi^*_{new} > \chi^*$.

and under some assumptions all three models are equivalent to one another. Only (KIN3) is coupled later with the transport model.

(KIN1). The model (16) from [30, 75] splits u(t) as a sum of the methane amount in the h phase and of the amount in the l phase, and prescribes the evolution

(KIN1)
$$\frac{d}{dt}((1-S)\chi) = -Q; R\frac{dS}{dt} = Q; Q = k_1(\chi - \chi^*); (\chi(0), S(0)) = (\chi^0, S^0).$$
 (18)

This model is very intuitive: in particular, we see that $S \uparrow$ when $\chi > \chi^*$. However, (KIN1) works well only in D_+^0 when $u^0 \geq \chi^*$, i.e., when the equilibrium point $S^{\infty} \geq 0$. When $u^0 < \chi^*$ since k_1 does not involve S, the model leads to an equilibrium outside D^0 with $S^{\infty} < 0$. Moreover, the corresponding numerical scheme requires solution of a nonlinear algebraic equation which must be done with some care; see Sec. 10.2.

(KIN2). Next we aim to improve (KIN1). We split $u = \chi + S(R - \chi) = \chi + \psi$, with $S = \frac{\psi}{R - \chi}$. The variable ψ interpreted as the "amount of methane stored in the hydrate phase over the saturated amount in liquid". Given initial data (χ^0, S^0) , we calculate $\psi^0 = S^0(R - \chi^0)$, and postulate the evolution

(KIN2)
$$\frac{d\chi}{dt} = -Q; \quad \frac{d}{dt}(\psi) = Q; \quad Q = k_2(\chi - \chi^*); \quad (\chi(0), \psi(0)) = (\chi^0, \psi^0).$$
 (19)

Now (KIN2) model is linear in χ and ψ , and Q is monotone in χ : the curves $\chi + \psi = u^0$ are simply the lines in the (χ, ψ) plane. These properties simplify the implementation and analysis. However, similarly as in (KIN1) Q involves properly only the equilibria on E_*^+ , and thus (KIN2) works well only in D_+^0 .

(KIN3). We modify (KIN2) so that when $u^0 < \chi^*$, Q leads to some equilibrium on E_*^- , but when $u^0 \ge \chi^*$, the model works identically to (KIN2) and leads correctly to some equilibrium on E_*^+ . An elegant way to do it is to replace χ^* in the definition of Q in (KIN2) by a selection $w \in w_*(\psi)$ which defaults to χ^* on E_*^+ . Here $w_* = e_*^{-1}$, and $e_* = r_*E_*$ is a rescaled version of E_* , with a fixed $r_* = R - \chi^*$. When $\psi > 0$, we have $w = \chi^*$, but when $\psi = 0$, $w \in [0, \chi^*]$. Also, $S \in E_*(\chi)$ is equivalent to $\psi \in e_*(\chi)$ and $\chi \in w_*(\psi)$. The (KIN3) model we implement and analyze reads

(KIN3)
$$\frac{d\chi}{dt} = -Q; \quad \frac{d}{dt}(\psi) = Q; \quad Q = k_3(\chi - w); \quad w \in w_*(\psi); \quad (\chi(0), \psi(0)) = (\chi^0, \psi^0).(20)$$

The solution (χ, ψ) and the selection w are unique. The exchange term Q is monotone in χ while -Q is monotone in ψ which make the analysis and implementation easy. As in (KIN2), at any point of time one can calculate S from ψ and χ .

We provide details on (KIN1), (KIN2) and (KIN3) in Sec. 10.2. These inform our analysis of methane transport coupled to (KIN3).

5. Approximation schemes for methane transport model under equilibrium or kinetic closure

We summarize now the methane transport model in a form amenable to discretization and analyses. First we outline how the thermodynamic conditions on (P, T) and χ^* are handled.

Assume known T(x,t), or solve an appropriate energy equation (21a) under some initial and boundary conditions.

Assume known P(x,t), q(x,t), or find these from (8) under some boundary conditions(21b)

Calculate
$$\chi^*(x,t) = \chi^*(P(x,t), T(x,t), \chi_{lS}(x,t))$$
(21c)

For kinetic model, parametrize $w_*(x,t)$ with $\chi^*(x,t)$.

For (21c) we use the approach described in [49] based on estimates of χ^* generated by CSMGem, semi-empirical model from [61], and the parametric model from [12] using algebraic curve fitting model for equilibrium pressure, P_{eq} , given in [38]. In examples for this paper we assume $\chi_{lS} = \chi_{lS}^{sw}$.

Next use mass conservation (5) which we divide by ρ_l upon (A3). The equilibrium model, with u(x,t) given by (11) is

$$\partial_t (\phi u) + \nabla \cdot (q\chi) - \nabla \cdot (d_m \nabla \chi) = \frac{F_M}{\rho_l}, \ x \in \Omega, t > 0,$$
 (22a)

$$\chi(x,t) = \min\{\chi^*(x,t), u(x,t)\},$$
 (22b)

$$u(x,0) = u_{init}(x), x \in \Omega.$$
 (22c)

Assume boundary conditions for
$$\chi(x,t)$$
, $x \in \partial \Omega, t > 0.$ (22d)

The kinetic model rewrites (22a) in terms of χ and ψ . To achieve a convenient symmetrized form, we replace $\partial_t(\phi u) = \phi \partial_t(\chi + \psi) = \phi \partial_t(\chi) + \phi Q$ with $Q = -k_3(w - \chi)$ given as in (20). The model completed with appropriate initial data for χ and ψ and boundary data for χ reads

$$\partial_t(\phi\chi) - \phi k_3(w - \chi) + \nabla \cdot (q\chi) - d_m \nabla^2 \chi = \frac{F_M}{\rho_l}, \quad x \in \Omega, t > 0,$$
 (23a)

$$\partial_t(\psi(x,t)) + k_3(w - \chi(x,t)) = 0, \ w \in w_*(x,t;\psi).$$
 (23b)

$$\chi(x,0) = \chi_{init}(x), \qquad \psi(x,0) = \psi_{init}(x), \quad x \in \Omega.$$
 (23c)

Assume boundary conditions for
$$\chi(x,t)$$
, $x \in \partial \Omega, t > 0$. (23d)

We comment now on the couplings. The models (22) and (23) are strongly coupled to the thermodynamic conditions given in (21c) and to the flux q found by (21b). For the time scales of interest in this paper, most significant are the parametrizations of (22b) and (23b) by the quantity $\chi^* = \chi^*(x,t)$ found in (21c). On the other hand, $\chi^*(x,t)$ depends primarily on the temperature and much less on P(x,t). At the same time, the conductivities in the energy equation are less sensitive to S than the quantities in the pressure equation; see, e.g., data in [35].

In turn, the solution to (21) depends on the solution to the methane transport (22) or (23). In particular, as (9) indicates, the local variations in q(x,t) are due to $\nabla \cdot q \approx \partial_t (\phi[S^{\frac{\Delta \rho}{\rho_t}}])$, which require re-computing q. In addition, the permeability K in (21b) depends on S, and the resulting local pressure variation may affect χ^* by the appearance of micro-cracks; see, e.g., [9, 44].

These inter-dependencies can be resolved by iteration, time-lagging, or variable freezing; we discuss these next.

5.1. Approximation schemes and resolving coupled components. The choice of time-stepping and spatial discretization depends on the objectives of simulation and on the competing demands of modeling accuracy, and efficiency and robustness of the solver. In this paper we are interested in modeling hydrate evolution in natural environment. The simulation scenarios we consider may involve response to changing boundary conditions for temperature or pressure such as due to the warming sea waters or sudden change in the sediment depth. We consider that these inputs vary in time on the scale of years or kiloyears but not as strongly as in production scenarios on the scale of days or hours. This assumption on the time scale motivate the choice of time stepping.

The simplest way to resolve the couplings is to consider the variables P(x) and T(x) as time-independent over the simulation time scale, i.e., "freeze them" over [0,T], and to solve the equilibrium model (22). This strategy is adopted in many hydrate models at basin scale where the pressure and temperature assumed known between any large geologic events and where P(x), T(x) follow closely the hydraulic gradient and geothermal gradient, respectively; see, e.g., [49, 50, 62]. For simulation over shorter time scales this approach may require recomputing P(x) and T(x) over shorter time frames whenever the external controls change. With the equilibrium model (22), the system is immediately brought to equilibrium in the first transport step. To simulate a gradual return to equilibrium, we must use the kinetic model (23).

The most complex and comprehensive way to resolve the couplings is to use fully implicit coupling for the equilibrium model [35] and for the kinetic model [17, 18]; see also general subsurface simulators described in [68]. However, a fully implicit solution for several independent variables including phase behavior requires delicate time-stepping with advanced strategies to ensure global convergence and robustness of the Newton solver.

As an intermediate strategy between the most complex and most simple, the coupling including the evaluation of thermodynamic conditions can be handled in a sequential manner or by time-lagging. Our analysis applies in this setting. Here (21) is solved at (almost) every time step. Once (P, T, χ^*) are known, (22) or (23) follow. This is similar to a strategy common in reservoir simulation and compositional models called IMPES or IMPEC in which the pressure equation and thermodynamics conditions in (21) and the concentration equations (22) are solved at separate time schedules with large pressure time steps ΔT , and small transport steps $\tau = \Delta T/K$. See, e.g., [41, 47, 67] where K > 1 was used. The sequential and time-lagging strategies carry some modeling error compared to the fully implicit model; the error decreases when small time steps are used. Additional iterations to decrease this error can be carried out over the macro time step; see recent analysis on multi-rate schemes for coupled flow and geomechanics in [3, 18]; additionally, stabilization terms may improve convergence in [27, 51]. If needed, we can also set K = 1 and $\tau = \Delta T$.

In our computational model we follow the time lagging strategy with macro-time steps but without iteration. We tested this strategy for hydrate basin modeling in [50]. For simplicity below we assume uniform time stepping.

5.2. Time-stepping with macro time steps and concentration time steps. The concentration time step $\tau = \frac{T}{N}$ for (22) or (23) is chosen to satisfy some stability constraints. The macro time step $\Delta T = K\tau$ for (21) is chosen to be small enough so that $\chi^*(x,t), q(x,t)$ respond to the model inputs for pressure and temperature. Here $K \geq 1$. Now MK = N

and $T = M\Delta T = MK\tau = N\tau$.

$$0 = t^0 < t^1 < \dots < t^n = n\tau < \dots < t^N = T = N\tau$$
, with $t^n = n\tau$, $n = 0, 1, \dots, N$.
 $0 = T^0 < T^1 < \dots < T^m = m\Delta T < \dots < T^M = T = M\Delta t$, with $m = 0, 1, \dots, M$.

Note that $T^m = m\Delta T = mK\tau = t^{mK}$. We outline our algorithm.

```
Time stepping (macro time steps) m=1,2,\ldots M. (Macro-time step [T^{m-1},T^m]):

Assume S|_{T^{m-1}} is known. Recalculate hydraulic properties.

Solve (21) for (T,P,q,\chi^*)|_{T^m}.

Set the values (q,\chi^*),t\in[T^{m-1},T^m] from (q,\chi^*)|_{T^m} or by interpolating between these and (q,\chi^*)|_{T^{m-1}}.

(Concentration time steps n=(m-1)K+1\ldots mK):

Assume (q,\chi^*),t\in[T^{m-1},T^m]=[t^{(m-1)K},t^{mK}] known.

Solve in each [t^{n-1},t^n] the concentration problem (22) or (23) for (S,\chi)|_{t^n}.

With n=mK, set S|_{T^m}=S|_{t^n}. Advance to the next macro-time step with m:=m+1.
```

We devote Ex. 5 in Sec. 8.3 to the study of sensitivity of simulations to ΔT .

5.3. **Spatial discretization.** We set up hexahedral grid over Ω and use finite volume type approximations. Our schemes are first-order in time, with explicit in time upwind treatment of advection, and implicit treatment of phase behavior and diffusion at every time step. For simplicity we define the schemes for 1d case with $x \in \Omega = (0, D^{max})$ with x = 0 at or above BHSZ, and x pointing upwards, with the flux upwards q(x,t) > 0. We cover Ω with uniform size grid cells $[x_{j-1/2}, x_{j+1/2}]$, each with center at $x_j = (j+1/2)h$ where $h = x_{j+1/2} - x_{j-1/2}$. We denote the grid values $V_j \approx v(x_j)$, and $V_j^n \approx v(x_j, t^n)$. The Darcy flux q are defined at the cell edges $q_{j\pm 1/2}^n$. The fluxes χq are approximated as is done for the space-dependent flux in the "color equation" [32][Chapter 9].

We skip the presentation of schemes for (21) which are standard; see, e.g., [35, 46]. However, our treatment of phase equilibria and of kinetics requires care. In Sec. 6 we define numerical schemes for the concentration steps (22) and in Sec. 7 for (23). These share the mass conservation equation discretized as follows. We approximate $U_j^n \approx u(x_j, t^n)$ and $X_j^n \approx \chi(x_j, t^n)$ discretizing the mass conservation (22a) and (23a) parts of (22) and (23) by

$$\phi_j(U_j^n - U_j^{n-1}) + \frac{\tau}{h}(q_{j-1/2}^{n-1}X_j^{n-1} - q_{j-3/2}^{n-1}X_{j-1}^{n-1}) + \frac{d_m\tau}{h^2} \left[2X_j^n - X_{j-1}^n - X_{j+1}^n \right] = \frac{\tau F_M(x_j, t^n)}{\rho_l}.(24)$$

We approximate the initial data $U_j^0 = \frac{1}{h} \int_{x_{j-1/2}}^{x_{j+1/2}} u_{init}(x) dx$. The initial data for (χ, ψ) in the approximation to (23) is defined analogously.

The equation (24) is complemented with the discrete version of (22b) for the equilibrium model or with discrete version of (23b) for the kinetic model, and with appropriate statement on the boundary conditions. These are stated in Sec. 6 and 7 along with the analysis of their stability.

6. Stability analysis for equilibrium model

We first recall notation. For some grid function $V = (V_j)_j$ with $V_j \approx v(x_j)$, and $V^n = (V_j^n)_j$, we let V^{Δ} represent the collection of all $(V^n)^n$. We recall $||V||_1 = h \sum_j |V_j|$, and the total variation $TV(V^n)$ and total variation in time $TV_T(V^{\Delta})$ defined as

$$TV(V^n) = \sum_{j \in \mathbb{Z}} |V_j^n - V_{j-1}^n|, \quad TV_T(V^{\Delta}) = \sum_{n=0}^{T/\tau} [\tau TV(V^n) + ||V^n - V^{n-1}||_1].$$

For the kinetic problem we work with $\|(X^n, \Psi^n)\|_{\Delta,1} = \|X^n\|_{\Delta,1} + \|\Psi^n\|_{\Delta,1}$, and $TV(X^n, \Psi^n)$ and $TV_T(X^\Delta, \Psi^\Delta)$ extended similarly to product space. In our analysis we study $TV_T(U^\Delta)$ for (22) and $TV_T(X^\Delta, \Psi^\Delta)$ for (23). These quantities help to predict the variability and challenges to the numerical solution depending on the data. We show that $TV_T(U^\Delta)$ and $TV_T(X^\Delta, \Psi^\Delta)$ increase in time depending on the variability and smoothness of initial data $\chi^*(x,t)$ and q(x,t) in x and t. Stability along with consistency of the discrete schemes lead to the convergence of numerical schemes. Our analysis is also useful to understand the sensitivities of the models (22) and (23) on their data.

(AA)Assumptions for analysis. We analyze only the scheme (24) for transport model complemented by an equilibrium or kinetic closure to be stated, under assumptions (A1-A5). We assume that the data $\chi^*(x,t)$ and q(x,t) found by (21) is known over each macro-time step $[T^{m-1},T^m]$ and varies in some predictable fashion. As usual, to study the accumulation of the discretization error in time, we set $F_M=0$. We also set set $d_m=0$ to focus on the advection dominated case. We consider the transport problem on $x \in \mathbb{R}$ (that is, $j \in \mathbb{Z}$) rather than $x \in \Omega$, which avoids dealing with a mixture of boundary and initial conditions in the analysis. For this we assume that initial data and the solution to the transport problem have compact support in some $\Omega_S \subset \mathbb{R}$ with measure ω_S , and this reduces summing over $j \in \mathbb{Z}$ to $j \in \mathbb{Z}^0$. Clearly, realistic simulations consider a bounded domain and boundary conditions.

Finally, we assume the sediment is homogeneous with $\phi(x) = \phi_0 = const$, and we drop ϕ_0 while keeping the notation unchanged, but the analysis could be amended easily as long as $\phi(x)$ is smooth and bounded away from 0. In particular, in (22) we could change variables and set $\overline{u} = u(x,t)\phi(x)$ with $\chi(x,t) = \min\{\chi^*(x,t), \frac{\overline{u}(x,t)}{\phi(x)}\}$.

We now restate (24) under the assumptions (AA) amended by the discrete version of (22b)

$$\frac{1}{\tau}(U_j^n - U_j^{n-1}) + \frac{\tau}{h}(q_{j-1/2}^{n-1}X_j^{n-1} - q_{j-3/2}^{n-1}X_{j-1}^{n-1}) = 0, \quad X_j^n = \min\{\chi^*(x_j, t^n), U_j^n\}, \quad j \in \mathbb{Z}^0. (25)$$

We analyze this scheme recognizing its familiar upwind character

$$U_j^n = U_j^{n-1} - \frac{\tau}{h} \left[F_j^{n-1} - F_{j-1}^{n-1} \right], \quad F_j^{n-1} = q_{j-1/2}^{n-1} X_j^{n-1} = f(x_j, t^{n-1}; U_j^{n-1})$$
 (26)

for a conservation law with the flux function f(x,t;u) which we set from (5) under (AA)

$$\partial_t u + \partial_x f = 0; \text{ for } x \in \mathbb{R}, t \in [0, T)$$
 (27a)

$$f(x,t;u) = q(x,t)\chi(x,t) = q(x,t)\min\{\chi^*(x,t), u(x,t)\},$$
(27b)

$$u(x,0) = u_{init}(x). (27c)$$

The function f is illustrated in Fig. 3 for a typical homogeneous unconsolidated sand reservoir with data from Ulleung Basin [49], with x pointing upwards and $q(x,t) \approx const > 0$.

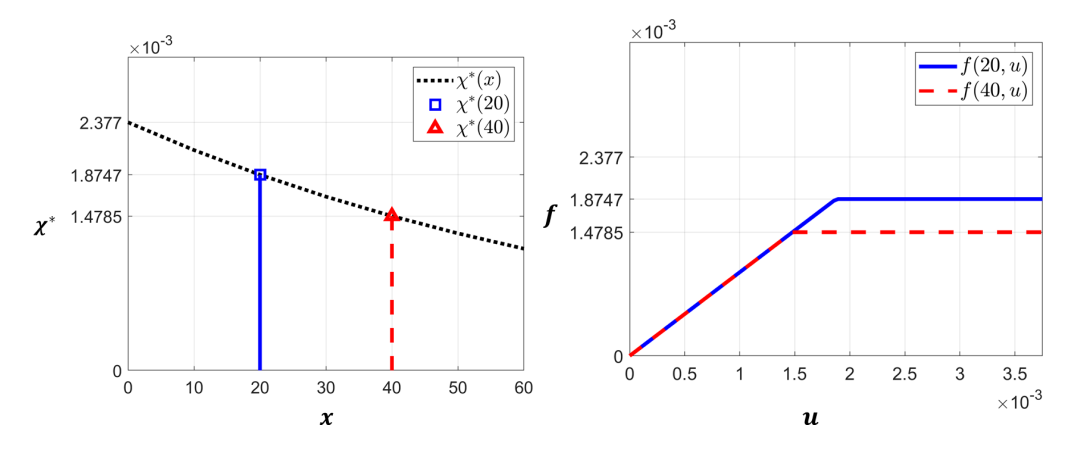


FIGURE 3. Illustration of $\chi^*(x)$, and of the flux function f(x;u) with data from Ulleung Basin case UBGH2-7 [49]. Left: typical $\chi^*(x)$ in homogeneous sediment, with values $\chi^*(x)$ highlighted at x=20, and x=40. Right: the flux function f(x;u) for x=20, and x=40. Note that the flux function f(x,t;u)is piecewise linear in u and features a corner at $u = \chi^*(x^*)$.

For stability of (26) when f = f(u) proving a bound for $TV_T(U^{\Delta})$ is usually the first step in the analysis of convergence [31, 32]; the first-order upwind scheme (26) converges at the rate of $O(\sqrt{h})$ in L^1 [28, 29, 59], the best possible convergence rate in the presence of discontinuities [55].

However, when f = f(x; u), the solutions to $u_t + f_x = 0$ do not in general obey the maximum principle, and its quasilinear form $u_t + f_u(x;u)u_x = -f_x(x;u)$ with $|f_x| \leq L_f$ reveals that the solution may grow pointwise as $O(L_f t)$ while its total variation may grow in time; see the discussion in [32] [Chapter 9] and [24, 25, 63]. Under some assumptions the analysis in [37] predicts that $TV(U^n)$ found with Godunov scheme grows linearly in time, but these assumptions are not applicable to (25).

We formulate therefore our own auxiliary stability result for (26) similar to those known, e.g., from [32]. Surprisingly, we did not find it stated in literature, thus we provide detailed proof in Sec. 10.1.

Proposition 1. Consider (27) and assume suppose that $f \in C_b^2(\overline{\Omega} \times \mathbb{R}_+ \times \mathbb{R})$ and is nondecreasing in u. Let the time step size τ be small enough so that

$$\max_{(x,t,u)} \left| \frac{\tau}{h} f_u(x,t;u) \right| \le 1. \tag{28}$$

Let also some initial data U^0 be given, with bounded variation, and let also U^{Δ} be the solution to (26) with compact support of measure bounded by ω_S . Let also

$$L_{1} = \max_{(x,t,u)} \{ |f_{xu}(x,t;u)|, |f_{xx}(x,t;u)| \}; \quad L_{2} = \max_{(x,t,u)} \{ |f_{u}(x,t;u)|, |f_{x}(x,t;u)| \}.$$
 (29)

Then we have for all n > 0

$$TV(U^n) \le C_1(T) = TV(U^0)e^{TL_1} + 2\omega_S(e^{TL_1} - 1),$$
 (30a)

$$||U^{n+1} - U^n||_1 \le \tau C_2(T), \quad C_2(T) = L_2(C_1(T) + \omega_S),$$
 (30b)

$$TV_T(U^{\Delta}) \le C_3(T) = T(C_1(T) + C_2(T)).$$
 (30c)

To apply Proposition 1 to (25), we consider f(x, t; u) defined in (27b) depending on the physical data q, χ^* . We see that $f(\cdot; u)$ is continuous nondecreasing and piecewise linear in u and differentiable except where $u(x, t) = \chi^*(x, t)$. Since f is at best piecewise smooth in u, Proposition 1 applies only to some regularization of (27)

$$u_t^{\epsilon} + f^{\epsilon}(x, t; u^{\epsilon})_x = 0, \quad u^{\epsilon}(x, 0) = u_{init}(x), \tag{31}$$

in which f is approximated with some C^2 smooth, positive nondecreasing function f^{ϵ} . Since we can make $f^{\epsilon} \approx f$ arbitrarily close, we trust that (31) closely resembles (27); we illustrate this regularization in Ex. 2 in Sec. 8.

Next question is whether the assumptions on f^{ϵ} itself are reasonable for a real hydrate reservoir simulation. First, the problem (27) is only a simplification of the strongly coupled dynamical problem (21)–(22), and our stability analysis does not explain or refer to the strength of the couplings. Instead, we make a-priori assumptions on the data which allow to conclude stability and predict the variability of solutions. In particular, we predict variability of u quantified by $TV_T(U^{\Delta})$ depending on the constants L_1, L_2 given in (29); these are small only when q, q_x , the lithology and χ^* vary smoothly. We discuss this in detail below.

6.1. Assumptions required for the stability of (25) in a hydrate reservoir. From the form of (27) and properties of f, we expect its solution u(x,t) to feature a family of right and left states travelling at different speeds due to the "corner" of f at $u = \chi^*$. In particular, the speed of the state for any $u > \chi^*$ is zero; this leads to S > 0, i.e., the growth of immobile amount of methane trapped as solid hydrate with the appearance of sharp bands of hydrate. We rewrite (31) as

$$u_t^{\epsilon} + f_u^{\epsilon}(x, t; u^{\epsilon})u_x^{\epsilon} = -f_x^{\epsilon}(x, t; u^{\epsilon}), \tag{32}$$

which illustrates that the solution $u \approx u^{\epsilon}$ and the corresponding $S \approx S^{\epsilon}$ grow along its characteristics with a rate bounded by the source $-f_x^{\epsilon}$. To quantify, we define

$$L_{q} = \max_{(x,t)} |q(x,t)|; \ L_{q_{x}} = \max_{(x,t)} |q_{x}(x,t)|; \ L_{\chi^{*}} = \max_{(x,t)} |\chi_{x}^{*}(x,t)|; \ L_{3} = \max_{(x,t)} |\chi_{t}^{*}(x,t)|.$$
(33)

Remark 2. Assume that χ^* and q vary mildly so that L_1, L_2, L_{χ^*} are finite and that

$$\frac{\tau}{h}L_q \le 1,\tag{34}$$

so that (28) holds. Then the scheme (25) for the equilibrium model is weakly stable.

We comment now on the constants L_1, L_2, L_{χ^*} in realistic reservoirs. Assume first the quasi-static case in a homogeneous reservoir with P(x) and T(x) fixed in time t, and with $0 < q = L_q$. In this case $||f_x||_{\infty} = L_q L_{\chi^*}$. Consider for example $\chi^*(x) = a \exp(-bx)$ from [49] given with some a > 0 and small b > 0. Now $L_{\chi^*} = ab$, $f_x < 0$, $||f_x||_{\infty} = L_q ab$ and $L_1 = ||f_{xx}||_{\infty} = L_q ab^2$ is small. In turn, we can check that $L_2 = L_q \max(1, ab)$. These stability constants correlate well with the predictions of hydrate band growth in nature which are large when q is large.

Consider next heterogeneous reservoirs. Here the maximum solubility $\chi^*(x)$ depends on the type of sediment, e.g., in grain size [9]. Consequently, close to some interfaces between different sediment layers, hydrate can accumulate much faster than elsewhere [9, 52, 64]. The locally high hydrate accumulation can be predicted from (32), since at a discontinuity of χ^* , its weak derivative $\partial_x \chi^*$ is a Dirac term which may cause a dramatic local increase of U_i^* and of the saturation. We illustrate this later in Ex. 3 in Sec. 8.

Finally, we consider the time dependent case closest to the strongly coupled hydrate systems when q = q(x,t) and $\chi^* = \chi^*(x,t)$ and when T = T(x,t) and P = P(x,t). Now the magnitude of f_x comes from both $q_x\chi^*$ and $q\chi_x^*$ which may have opposite signs and disparate magnitudes depending, e.g., on the solutions of (9). It is hard to predict these a-priori, and we can only make assumptions that the constants in Remark 2 are bounded. Simulation with $\chi^* = \chi^*(x,t)$ which varies in time is considered in Ex. 5 in Sec. 8.

This discussion completes our analysis of the equilibrium case. Based on Proposition 1, we expect the rate of convergence $O(\sqrt{h})$ for the solutions to (25); this is confirmed by numerical experiments in Sec. 8.

7. Scheme for kinetic model and its stability

Now we consider a numerical scheme for the kinetic model (23). We implement the general case with source terms and diffusion and approximate $\chi(x_j,t^n)\approx X_j^n$ and $\psi(x_j,t^n)\approx \Psi_j^n$, with $U_j^n = X_j^n + \Psi_j^n$. Given $(X_j^{n-1}, \Psi_j^{n-1})$ we find (X_j^n, Ψ_j^n, W_j^n) as solutions to the local nonlinear system at every j; in this local problem the kinetic terms Q_j^n are handled implicitly. We set $k = \tau k_3$. The scheme (24) under assumptions (AA) in the form directly amenable to analysis reads

$$(X_{j}^{n} - X_{j}^{n-1}) - k(W_{j}^{n} - X_{j}^{n}) + \frac{\tau}{h}(q_{j-1/2}^{n-1}X_{j}^{n-1} - q_{j-3/2}^{n-1}X_{j-1}^{n-1}) = 0,$$

$$(\Psi_{j}^{n} - \Psi_{j}^{n-1}) + k(W_{j}^{n} - X_{j}^{n}) = 0, \quad W_{j}^{n} \in w_{*}(x_{j}; \Psi_{j}^{n}35b)$$

$$(35a)$$

In practice we solve (35) as follows, denoting $\tilde{k} = \frac{k}{1+k}$. Given previous time step values $(X_j^{n-1}, \Psi_j^{n-1})_j$, at every j we solve for (X_j^n, Ψ_j^n) the local nonlinear system

$$X_j^n - k(W_j^n - X_j^n) = F_j^n, \quad F_j^n = X_j^{n-1}(1 - \frac{\tau}{h}q_{j-1/2}^{n-1}) + \frac{\tau}{h}q_{j-3/2}^{n-1}X_{j-1}^{n-1},$$
 (36a)

$$\Psi_j^n + k(W_j^n - X_j^n) = G_j^n, G_j^n = \Psi_j^{n-1}, W_j^n = w_*(x_j; \Psi_j^n).$$
 (36b)

This is a 2×2 nonlinear stationary system of equations with a maximal monotone graph w_* . It is uniquely solvable with the following explicit formulas which follow from Sec. 2. Since (36a) is linear in X_j^n , we can formally calculate $X_j^n = \frac{1}{1+k}(F_j^n + kW_j^n)$. After we plug this to (36b) we get $\Psi_j^n + \widetilde{k}w_*(\Psi_j^n) = G_j^n + \widetilde{k}F_j^n$. Applying the resolvent $\mathcal{R} = \mathcal{R}_{\widetilde{k}}^{w_*} = (I + \widetilde{k}w_*)^{-1}$ of w_* we obtain $\Psi_j^n = \mathcal{R}(G_j^n + \widetilde{k}F_j^n)$. We substitute to get W_j^n and X_j^n . Finally we can calculate the saturations $S_j^n = \frac{\psi_j^n}{R - X^n}$.

For stability of the scheme we need an auxiliary result formulated for (36) with indices dropped and with inputs F, G and outputs X, Ψ .

Lemma 1. Consider (36) with the right hand side (F,G) and solutions (X,Ψ,W) . Consider also the right hand side $(\overline{F}, \overline{G})$ with the corresponding solutions $(\overline{X}, \overline{\Psi}, \overline{W})$ to (36). The following comparison principle and stability hold

$$|X - \overline{X}| + |\Psi - \overline{\Psi}| \le |F - \overline{F}| + |G - \overline{G}|.$$
 (37a)

$$|X| + |\Psi| \le |F| + |G|. \tag{37b}$$

We also have $W - \overline{W} = \frac{1}{k}(G - \overline{G}) + (\Psi - \overline{\Psi})(1 - \frac{1}{k}).$

Proof. The result (37a) is a special case in $\mathbb{R} \times \mathbb{R}$ of the result, in [21] for a(u) + c(u - v) = f; b(v) - c(u - v) = g, where $a(\cdot)$ is maximal monotone, $b(\cdot)$ is strongly monotone and continuous, and $c(\cdot)$ is maximal monotone single valued. The stability result (37b) follows from the comparison principle (37a). In turn, the algebraic formula for $W - \overline{W}$ follows directly from algebra.

7.1. **TV-stability for the kinetic scheme** (36). Now we prove properties of (36). Throughout we assume that the CFL condition (34) holds and that the constants L_3 , L_{χ^*} are finite. First we apply the stability part of Lemma 1 directly to (36) to obtain

$$\left| X_{j}^{n} \right| + \left| \Psi_{j}^{n} \right| \leq \left| X_{j}^{n-1} \right| \left(1 - \frac{\tau}{h} q_{j-1/2}^{n-1} \right) + \frac{\tau}{h} q_{j-3/2}^{n-1} \left| X_{j-1}^{n-1} \right| + \left| \Psi_{j}^{n-1} \right|. \tag{38}$$

Multiplying by h and summing both sides over $j \in \mathbb{Z}^0$, and collapsing the first two terms on the right hand side, we obtain the stability result. We obtain that scheme (36) is stable in the product space

$$\|(X^n, \Psi^n)\|_{\Delta,1} \le \|(X^{n-1}, \Psi^{n-1})\|_{\Delta,1}. \tag{39}$$

Next we prove weak TV-stability which reveals the dependence of $w_* = w_*(x_i;\cdot)$ on x_i .

Proposition 2. Assume $\chi^*(x)$ is smooth so that L_3 and L_{χ^*} given by (29) are finite. Assume also $(X^{\Delta}, \Psi^{\Delta})$ have compact support with measure bounded by ω_S . If CFL condition (34) holds, then

$$TV(X^n, \Psi^n) \le TV(X^0, \Psi^0) + C_4T, ; C_4 = 2k_3\omega_S L_{\chi^*}.$$
 (40)

Proof. We write the system (36) at j and at j-1 and at t^n . We set $\Psi = \Psi_j^n$ and $\overline{\Psi} = \Psi_{j-1}^n$, with analogous notation for other variables, and consider

$$X - kW + kX = F, (41a)$$

$$\Psi + kW - kX = G; W \in w_*(\Psi), \tag{41b}$$

$$\overline{X} - k\overline{W} + k\overline{X} = \overline{F}, \tag{41c}$$

$$\overline{\Psi} + k\overline{W} - k\overline{X} = \overline{G}; \ \overline{W} \in v_*(\overline{\Psi}).$$
 (41d)

Here for shorthand we denoted the graph $w_*(x_j, t^n)$ by w_* and a different graph $w_*(x_{j-1}, t^n)$ at x_{j-1} by $v_*(\cdot)$. Since the graphs w_* and v_* are not the same, we cannot directly apply Lemma 1. Instead, we rewrite the third and fourth equations with w_* instead of v_* , move the difference between w_* and v_* to the right hand side, and examine the difference $w_* - v_*$ due to their "height", respectively, $\chi^*(x_j, t^n)$ and $\chi^*(x_{j-1}, t^n)$.

For $\psi > 0$ we can write

$$v_*(\psi) = w_*(\psi) - A_j h, \ \psi > 0, \ A_j = \frac{d}{dx} \chi^*(\overline{x}_j, t^n), \ \overline{x}_j \in (x_{j-1}, x_j).$$

When $\psi = 0$ both w_* and v_* are set-valued, and we must work with their Yosida approximations w_{λ} and v_{λ} . In fact for small ψ we have $w_{\lambda}(\psi) = v_{\lambda}(\psi)$, while for any ψ and λ we have $v_{\lambda}(\psi) = w_{\lambda}(\psi) - A_{i}(\lambda; \psi)h$, with $|A_{i}(\lambda; \psi)| \leq L_{\chi^*}$ from (33).

Reconsidering (41) with v_{λ} and w_{λ} instead of v_{*} and w_{*} but keeping the notation unchanged otherwise, we calculate $k\overline{W} = kv_{\lambda}(\overline{\Psi}) = kw_{\lambda}(\overline{\Psi}) - khA_{j}$, and the third and fourth equations

read now

$$\overline{X} - kw_{\lambda}(\overline{\Psi}) + k\overline{X} = \widetilde{F} = \overline{F} - khA_{j}(\lambda; \overline{\Psi}),$$

$$\overline{\Psi} + kw_{\lambda}(\overline{\Psi}) - k\overline{X} = \widetilde{G} = \overline{G} + khA_{j}(\lambda, \overline{\Psi}).$$

We can now apply the comparison Lemma 1 for the maximal monotone w_{λ} and inputs $F, G, \widetilde{F}, \widetilde{G}$. We apply the uniform bound on A_j in (37a), notice $\left|\widetilde{F} - F\right| \leq \left|\overline{F} - F\right| + khL_{\chi^*}$ and $\left|\widetilde{G} - G\right| \leq \left|\overline{G} - G\right| + khL_{\chi^*}$. Taking the limit as $\lambda \to 0$ we obtain, reverting back to the original notation of (36) that

$$\left| X_{j}^{n} - X_{j-1}^{n} \right| + \left| \Psi_{j}^{n} - \Psi_{j-1}^{n} \right| \leq \left| X_{j}^{n-1} - X_{j-1}^{n-1} \right| \left(1 - \frac{\tau}{h} q_{j-1/2}^{n-1} \right) + \left| \frac{\tau}{h} q_{j-3/2}^{n-1} \right| \left| X_{j-1}^{n-1} - X_{j-2}^{n-1} \right| + \left| \Psi_{j}^{n-1} - \Psi_{j-1}^{n-1} \right| + 2khL_{\chi^{*}}.$$
 (42)

The term $2khL_{\chi^*}$ will accumulate giving weak rather than strong stability. Summing (42) over those $j \in \mathbb{Z}^0$ with $\sum_j h \leq \omega_S$, we collapse the first two terms on the right hand side, and with $k = \tau k_3$ we get

$$TV(X^n, \Psi^n) \le TV(X^{n-1}, \Psi^{n-1}) + 2\tau k_3 \omega_S L_{\chi^*}.$$
 (43)

Applying recursively, we obtain (40) with $C_4 = 2k_3\omega_S L_{\chi^*}$.

Remark 3. The weak TV-stability result (40) in the product space for the kinetic problem (23) is similar to the weak stability (30a) we obtained for U^{Δ} in the equilibrium model (27), with the difference in the constants depending on $\chi^*(x)$, and the absence of the factor $(1+\tau L_1)$ in (43) in the product space.

7.2. **TV stability in time.** Given the known $(X_j^{n-1}, \Psi_j^{n-1})_j$ the next goal is to bound the terms $X_j^n - X_j^{n-1}$ and $\Psi_j^n - \Psi_j^{n-1}$. For this, we need a handle on $Q_j^n \propto W_j^n - X_j^n$ which quantifies the discrepancy from the equilibrium. We estimate Q_j^n in terms of Q_j^{n-1} .

Lemma 2. Under the assumption of Proposition 2 we have that

$$||Q^n||_1 \le C_5(T).$$

To prove the lemma, we estimate the terms in a regularized version of (36). Additional challenge is to allow for possible variability of w_* in time. We consider some smooth single valued approximations w_{λ} of $w_*|_{x_j,t^n}$ and v_{λ} of $w_*|_{x_j,t^{n-1}}$. The difference between these $w_{\lambda}(\psi) - v_{\lambda}(\psi) = B_j^n(\psi)\tau$ can be estimated uniformly in ψ with $|B_j^n| \leq L_3$, where L_3 is given in (33).

Proof. We rearrange (36), drop j, and seek the solution $(X_{\lambda}^n, \Psi_{\lambda}^n)$ to the regularized problem

$$X_{\lambda}^{n} - X^{n-1} - kQ_{\lambda}^{n} = F^{n-1},$$
 (44a)

$$\Psi_{\lambda}^{n} - \Psi^{n-1} + kQ_{\lambda}^{n} = 0, \tag{44b}$$

where $Q_{\lambda}^n=w_{\lambda}(\Psi_{\lambda}^n)-X_{\lambda}^n$ and $F^{n-1}=-\frac{\tau}{h}q_{j-1/2}^{n-1}X_{j}^{n-1}+\frac{\tau}{h}q_{j-3/2}^{n-1}X_{j-1}^{n-1}$. To get the estimates for Q_{λ}^n in terms of $Q_{\lambda}^{n-1}=v_{\lambda}(\Psi^{n-1})-X^{n-1}$, we break the expression

$$w_{\lambda}(\Psi_{\lambda}^{n}) - v_{\lambda}(\Psi^{n-1}) = w_{\lambda}(\Psi_{\lambda}^{n}) - w_{\lambda}(\Psi^{n-1}) + w_{\lambda}(\Psi^{n-1}) - v_{\lambda}(\Psi^{n-1}) = b(\Psi_{\lambda}^{n} - \Psi^{n-1}) + B\tau.$$

Here $b = w'_{\lambda}(\widetilde{\Psi_{\lambda}}) \geq 0$ with some $\widetilde{\Psi_{\lambda}}$, and $B = B_j^n$ discussed above, with $|B| \leq L_3$. Now we multiply (44b) by b and subtract (44a) from (44b). Rearranging we obtain

$$Q_{\lambda}^{n}(1+k(1+b)) = Q^{n-1} - F^{n-1} + B\tau.$$

We take absolute value, note $b \ge 0$, and pass to the limit with λ , to obtain, bringing back the index j

$$(1+k)\left|\left.Q_{j}^{n}\right.\right| \leq \left|\left.Q_{j}^{n-1}\right.\right| + \left|\left.F_{j}^{n-1}\right.\right| + \tau \left|\left.B_{j}^{n}\right.\right|.$$

Here, with L_q and L_{q_x} defined in (33), $|F_j^{n-1}|$ is bounded above

$$\begin{aligned} \left| F_{j}^{n-1} \right| &= \frac{\tau}{h} \left| q_{j-1/2}^{n-1} X_{j}^{n-1} - q_{j-1/2}^{n-1} X_{j-1}^{n-1} + q_{j-1/2}^{n-1} X_{j-1}^{n-1} - q_{j-3/2}^{n-1} X_{j-1}^{n-1} \right|, \\ &\leq \frac{\tau}{h} L_{q} \left| X_{j}^{n-1} - X_{j-1}^{n-1} \right| + \tau L_{q_{x}} \left| X_{j-1}^{n-1} \right|, \\ &\leq \frac{\tau}{h} L_{q} \left(\left| X_{j}^{n-1} - X_{j-1}^{n-1} \right| + \left| \Psi_{j}^{n-1} - \Psi_{j-1}^{n-1} \right| \right) + \tau L_{q_{x}} \left(\left| X_{j-1}^{n-1} \right| + \left| \Psi_{j-1}^{n-1} \right| \right). \end{aligned}$$

Multiply both sides by h and sum over $j \in \mathbb{Z}^0$ with $\sum_{j \in \mathbb{Z}^0} h \leq \omega_S$. Then apply (39) and (40) to get

$$(1+k)\|Q^n\|_1 \leq \|Q^{n-1}\|_1 + \tau \left[L_q TV(X^{n-1}, \Psi^{n-1}) + L_{q_x}\|(X^{n-1}, \Psi^{n-1})\|_{\Delta, 1} + L_3 \omega_S\right],$$

$$\leq \cdots \leq \|Q^0\|_1 + T \left[C_6(T) + L_3 \omega_S\right],$$

where $C_6(T) = L_q(TV(X^0, \Psi^0) + C_4T) + L_{q_x} ||(X^0, \Psi^0)||_{\Delta, 1}$. With k > 0, we have completed the proof.

Lemma 3. Suppose (40) holds for (X, Ψ) . Then we have

$$||(X^n - X^{n-1}, \Psi^n - \Psi^{n-1})||_{\Delta,1} \le \tau C_7(T).$$

Proof. Rewrite (36) estimating in the form

$$|X_{j}^{n} - X_{j}^{n-1}| \leq k |Q_{j}^{n}| + \frac{\tau}{h} L_{q} |X_{j}^{n-1} - X_{j-1}^{n-1}| + \tau L_{q_{x}} |X_{j-1}^{n-1}|,$$

$$|\Psi_{j}^{n} - \Psi_{j}^{n-1}| \leq k |Q_{j}^{n}|.$$

Next we multiply by h, take the sum over $j \in \mathbb{Z}^0$ and add these to get

$$\begin{aligned} \|(X^n - X^{n-1}, \Psi^n - \Psi^{n-1})\|_{\Delta,1} &\leq \tau \left[2k_3 \|Q^n\|_1 + L_q TV(X^{n-1}, \Psi^{n-1}) + L_{q_x} \|(X^{n-1}, \Psi^{n-1})\|_{\Delta,1} \right], \\ &\leq \tau \left[2k_3 \|Q^n\|_1 + C_6(T) \right]. \end{aligned}$$

With (39), (40) and the estimates for Q from Lemma 2, we get

$$\|(X^n - X^{n-1}, \Psi^n - \Psi^{n-1})\|_{\Delta, 1} \le \tau C_7(T) = \tau \left[2k_3 \|Q^0\|_1 + (1 + 2k_3 T)C_6(T) + 2k_3 T L_3 \omega_S \right].$$

Combining Lemma 3 and (40), we conclude with this main result.

Proposition 3. Under hypotheses of Proposition 2 we have

$$TV_T(X^n, \Psi^n) \le C_8(T) = T[C_4T + C_7(T)].$$
 (45)

Here $C_4 = 2k_3\omega_S L_{\chi^*}$, $C_7(T) = [2k_3\|Q^0\|_1 + (1+2k_3T)C_6(T) + 2k_3TL_3\omega_S]$, and $C_6(T) = L_q(TV(X^0, \Psi^0) + C_4T) + L_{q_x}\|(X^0, \Psi^0)\|_{\Delta, 1}$.

As in equilibrium case discussed in Sec. 6.1, this stability result depends on the variability of q and χ^* and on the initial discrepancy from the equilibrium through the constants in (45).

8. Numerical examples

In this section we provide examples for equilibrium and kinetic models. Our goal is to confirm the theory and in particular demonstrate convergence of the schemes for reasonably realistic cases as well as to demonstrate the practical limitations. We set $\nu = L_q \frac{\tau}{h} < 1$, and consider only 1d simulations.

For the equilibrium model we compare the numerical solution obtained by our scheme (25) with an analytical solution and we study effects of regularization; we also confirm the rate of convergence of $O(\sqrt{h})$. We study also the kinetic model and scheme (23), illustrate its convergence and show the dependence of hydrate formation on the properties of the flux function f in (27), and in particular on its variability across heterogeneous sediments. We also compare the equilibrium and kinetic models: as expected, kinetic solution are close to the equilibrium solution as the kinetic exchange rate increases.

In the last examples in Sec. 8.3 we illustrate the sensitivity of the model to the choice of macro time steps ΔT from Sec. 5.2.

8.1. Examples for equilibrium model.

Example 1 (Model case for equilibrium model with analytical solution). Let $\Omega = (-1,3)$, R = 2, $\chi_L = 1$, q = 1, and the initial condition $u_{init}(x) = \chi_L H(x+1)H(-x)$ for (27) features a "box"-like profile. We consider $\chi^*(x) = e^{-0.5x}$ independent of time. For additional interest, we also consider $\chi^*(x) = 1 - 0.26x$.

The analytical solution to (27) with $u_{init}(x) = \chi_L H(-x)$ can be found in [48]. We modify it for the present case of "box" shaped $u_{init}(x)$

$$\chi(x,t) = \min\left(1, \frac{\chi^{*}(x)}{\chi_{L}}\right) u_{init}(x-qt),
S(x,t) = -\frac{\max(0, t - \frac{x}{q}) q \chi_{x}^{*}(x) \mathbb{1}_{G_{0}(t)}(x)}{R - \chi^{*}(x)},
u(x,t) = \chi(x,t) + (R - \chi^{*}(x)) S(x,t),$$

where $G_0(t) = \{x : x_L < x \le qt\}$ with x_L satisfying $\chi^*(x_L) = \chi_L$, the position where first hydrate formation is observed.

We apply scheme (25) to obtain $(U^{\Delta}, X^{\Delta}, S^{\Delta})$ at T = 1 with M = 100 and $\nu = 0.9$. Illustrations are provided in Fig. 4. We see that $(U^{\Delta}, X^{\Delta}, S^{\Delta})$ are close to the analytical solution (u, χ, S) . As U^{Δ} propagates to the right, X^{Δ} satisfies the constraint $X_j^n \leq \chi^*(x_j)$, and the undissolved methane produces $S_j^n > 0$, i.e., we see the "blow-up" behavior of U^{Δ} with S_j^n as expected.

Comparing the two cases of $\chi^*(x) = 1 - 0.26x$ and $\chi^*(x) = e^{-0.5x}$, we see that the magnitude of χ^*_x is more pronounced for the latter case. In U^{Δ} and S^{Δ} we see small rarefactions at the back of the traveling wave, typical for an increasing concave flux function such as f given by (27b).

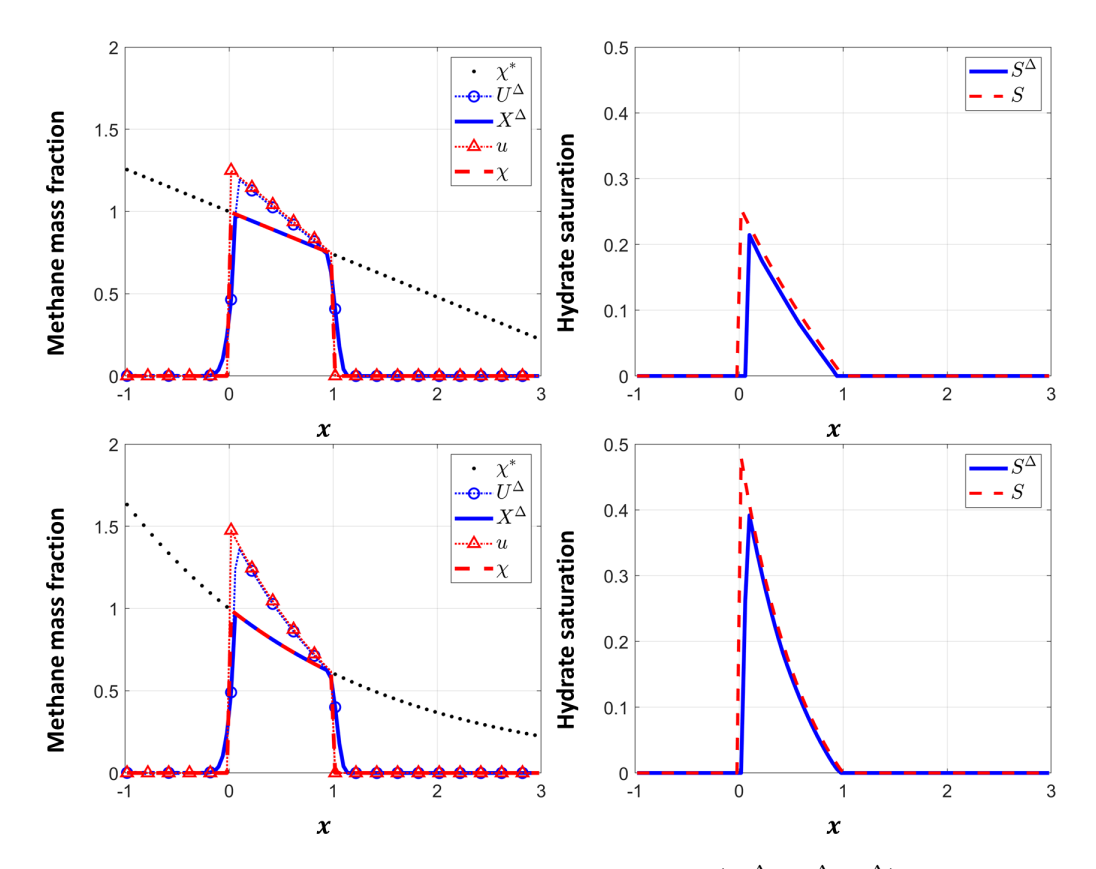


FIGURE 4. Comparison of the numerical solution $(U^{\Delta}, X^{\Delta}, S^{\Delta})$ with the analytical solution (u, χ, S) at T = 1 with M = 100 and $\nu = 0.9$ for Ex. 1. Top: case with for $\chi^*(x) = 1 - 0.26x$. Bottom: case with $\chi^*(x) = e^{-0.5x}$.

In our next example we evaluate effects of regularization in order to understand the closeness of u and u^{ϵ} , the solutions to (27) and (31). With f^{ϵ} chosen to be really close to f, we can make the difference between U^{Δ} and the solution to the regularized model $U^{\epsilon,\Delta}$ arbitrarily small. For comparison we use the case with the analytical solution from [48], which we adapt to the use of realistic data from Ulleung Basin.

Example 2. [Convergence rate and regularization; homogeneous domain, basin time scale] We consider (27) with $u_{init}(x) = \chi_L H(-x)$ on $\Omega = (0, D^{max})$ where D^{max} and χ^* are computed using the reference data measured from the Ulleung basin site UBGH2-7 of [49] with constant salinity of $\chi_{lS}^{sw} = 3.5\%$. Let $q = 5 \times 10^{-3} [\text{m/y}]$, $\chi_L = 2 \times 10^{-3}$, and R = 0.1203. We examine the result at T = 10 [ky].

The flux function f(x;u) given by (27b) has a corner at $u=\chi^*(x)$ at every x. We regularize with f^{ϵ} which replaces f on $(x,u) \in \Omega \times [\chi^*(x) - \epsilon, \chi^*(x) + \epsilon]$ by a smooth polynomial. Here ϵ is a regularization parameter; we choose $\epsilon = \alpha h$ with $\alpha = 10^{-4}$. In Fig. 5 we illustrate the analytical solution as well as the numerical solution $U^{\epsilon,\Delta}$ to the regularized problem, at t=10 kyrs with M=100 and $\nu=0.9$. We do not show U^{Δ} separately because it is virtually indistinguishable from $U^{\epsilon,\Delta}$.

We first examine the qualitative behavior. As predicted by the analytical solution, we observe the rapid growth of total methane content U^{ϵ} and the hydrate accumulation S^{ϵ}

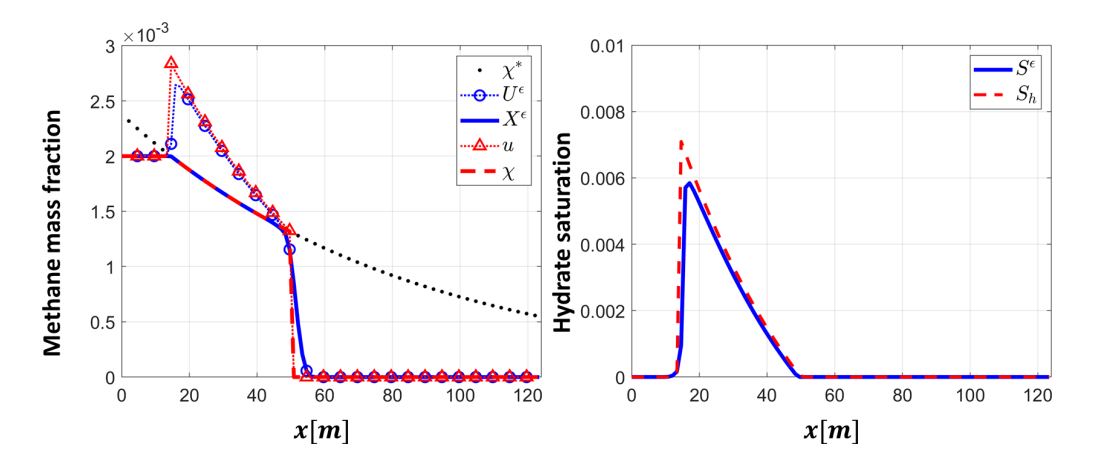


FIGURE 5. Numerical solution $(U^{\epsilon}, X^{\epsilon}, S^{\epsilon})$ of Ex. 2 at t = 10[ky] with M = 100 compared with the analytical solution (u, χ, S_h) .

because R < 1 while S^{ϵ} is inversely related to R. At t = 10 [ky], the hydrate saturation reaches about 10%.

Next we compare U^{Δ} and $U^{\epsilon,\Delta}$. With $\epsilon = O(h)$, their difference is small. In particular, when M = 100, $\|U^{\Delta} - U^{\epsilon,\Delta}\|_1 = 3.52 \times 10^{-4}$, $\|X^{\Delta} - X^{\epsilon,\Delta}\|_1 = 1.32 \times 10^{-4}$, and $\|S^{\Delta} - S^{\epsilon,\Delta}\|_1 = 2.20 \times 10^{-3}$. When M = 1000, $\|U^{\Delta} - U^{\epsilon,\Delta}\|_1 = 9.41 \times 10^{-6}$, $\|X^{\Delta} - X^{\epsilon,\Delta}\|_1 = 2.99 \times 10^{-6}$, and $\|S^{\Delta} - S^{\epsilon,\Delta}\|_1 = 5.46 \times 10^{-5}$.

We also check the rate of convergence using a fine grid solution with $100 \le M \le 6400$, plotted in Fig. 6.

$$||u - U^{\Delta}||_1 = O(h^{0.52}), \quad ||\chi - X^{\Delta}||_1 = O(h^{0.5}), \quad ||S - S^{\Delta}||_1 = O(h^{0.55}).$$

The order is similar for the solutions to the regularized model, with the error slightly bigger due to the modeling error. We have

$$||u - U^{\epsilon, \Delta}||_1 = O(h^{0.51}), \quad ||\chi - X^{\epsilon, \Delta}||_1 = O(h^{0.50}), \quad ||S - S^{\epsilon, \Delta}||_1 = O(h^{0.51}).$$

Our next example challenges the theory since it is set for heterogeneous sediment. This example is inspired by [9]; see our 2D simulation in [45] which accounts also for the flow and fracturing.

Example 3 (Model problem in heterogeneous domain motivated by [9]). Consider advection and diffusion of methane gas through 3 layers of sediments. Let $\Omega = \bigcup_{i=1}^{3} \Omega_i$ where i indicates each layer, each with different methane solubility curves: $\chi_1^*(x) = -0.3x + 1$, $\chi_2^*(x) = e^{-0.2(x-1)} - 0.2$ and $\chi_3^*(x) = -0.1x + 0.75$ shown in Fig. 7. We use R = 2, q = 1, $d_m = 0$ and $u_{init}(x) = 0.8H(-x)$.

The domain and the solutions are illustrated in Fig. 7 where the shaded blocks correspond to different layers. We focus on the behavior near the interfaces at x = 1 and x = 2. As the front of methane enters Layer 2 at x = 1, we expect to see methane hydrate dissociation since $\chi^*(1^+) > \chi^*(1^-)$ allows more methane gas to dissolve in the water. In contrast, at x = 2, there is a reduction in maximum solubility; $\chi^*(2^+) < \chi^*(2^-)$: this cause a sudden formation of hydrate at the interface as in [9, 52, 64]. The simulation captures the hydrate

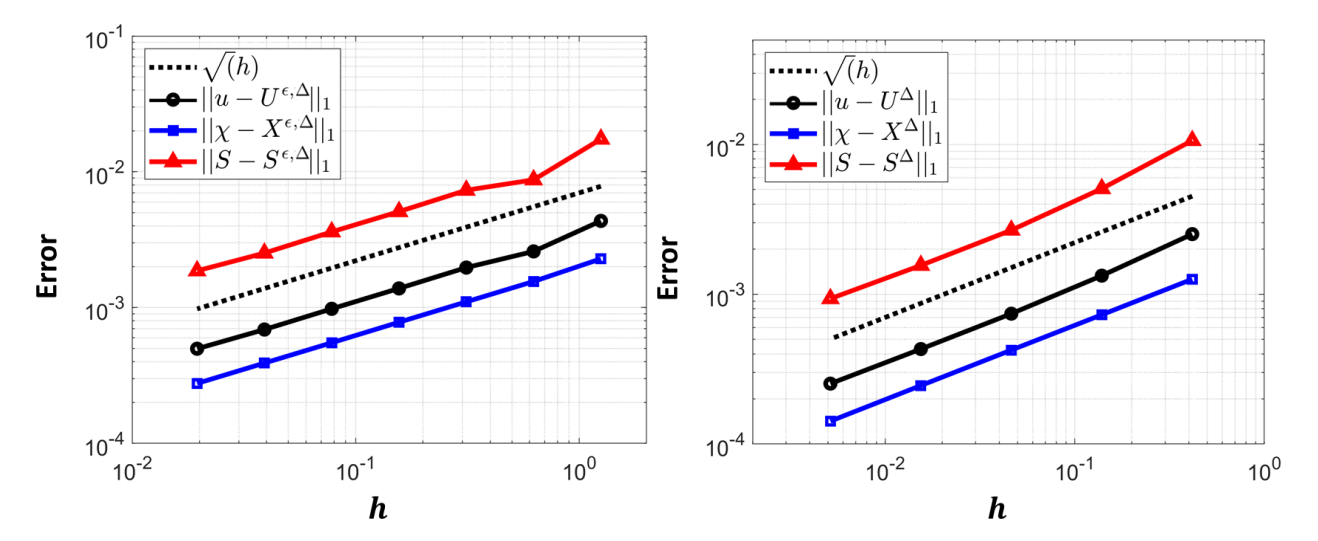


FIGURE 6. Left: L_1 -error between the numerical solution $(U^{\epsilon,\Delta}, X^{\epsilon,\Delta}, S^{\epsilon,\Delta})$ and the analytical solution (u, χ, S) at T = 10[ky]; from Ex. 2. Right: Convergence of the numerical solution $(U^{\Delta}, X^{\Delta}, S^{\Delta})$ to the analytical solution (u, χ, S) at T = 10[ky].

dissociation at x = 1 and the formation at x = 2. The sharp spike at x = 2 makes sense, since the weak derivative $\partial_x f(x, u)$ at the discontinuity at x = 2 is a Dirac source $\delta(x - 2)$.

8.2. Examples for kinetic model. Next we study convergence of the kinetic model, and compare the equilibrium model and kinetic models. Clearly kinetic rate should be fixed from experimental data; however, we can investigate the case as k_3 increases to see how realistic it is to use (KIN3) in place of equilibrium models. As k_3 increases, we see the solutions to (23) become closer to and eventually indistinguishable from those for the equilibrium model.

Example 4 (Model case: equilibrium and kinetic models). Let $\Omega = (0, 2), q = 1, R = 2$. We use $x_L = 0.35, \chi^*(x) = e^{-0.5x}$, and the initial condition $u_{init}(x) = \chi_L H(-x)$ with $\chi_L = 0.8395$. We simulate the problem using both the equilibrium model and scheme (26), and with the kinetic model and scheme (36) when $k_3 = 10$ and $k_3 = 100$. Here M = 100 and $\nu = q\tau/h = 0.9$. We compare with the equilibrium solution at T = 1.

Fig. 8 illustrates the results. We confirm that, as expected, the kinetic solution "lives" in the vicinity of the equilibrium solution. This closeness is more pronounced with larger k_3 . In turn, Fig. 9 shows that the numerical solutions $(U_{\text{KIN}}^{\Delta}, X_{\text{KIN}}^{\Delta}, S_{\text{KIN}}^{\Delta})$ converges to the fine grid solutions $(U_{\text{KIN,fine}}^{\Delta}, X_{\text{KIN,fine}}^{\Delta}, S_{\text{KIN,fine}}^{\Delta})$ at the order roughly of $O(h^{0.5})$.

$$\begin{split} \|U_{\rm KIN, fine}^{\Delta} - U_{\rm KIN}^{\Delta}\|_1 &= O(h^{0.57}), \\ \|X_{\rm KIN, fine}^{\Delta} - X_{\rm KIN}^{\Delta}\|_1 &= O(h^{0.56}), \\ \|S_{\rm KIN, fine}^{\Delta} - S_{\rm KIN}^{\Delta}\|_1 &= O(h^{0.62}). \end{split}$$

8.3. Equilibrium and kinetic schemes under varying environmental and thermodynamic conditions and sensitivity to macro steps. Finally we illustrate the dependence of the solutions to the equilibrium model and kinetic models depending on the choice of macro steps $T^m = m\Delta T$ at which χ^* is recomputed. We allow P = P(x, t) and T = T(x, t)

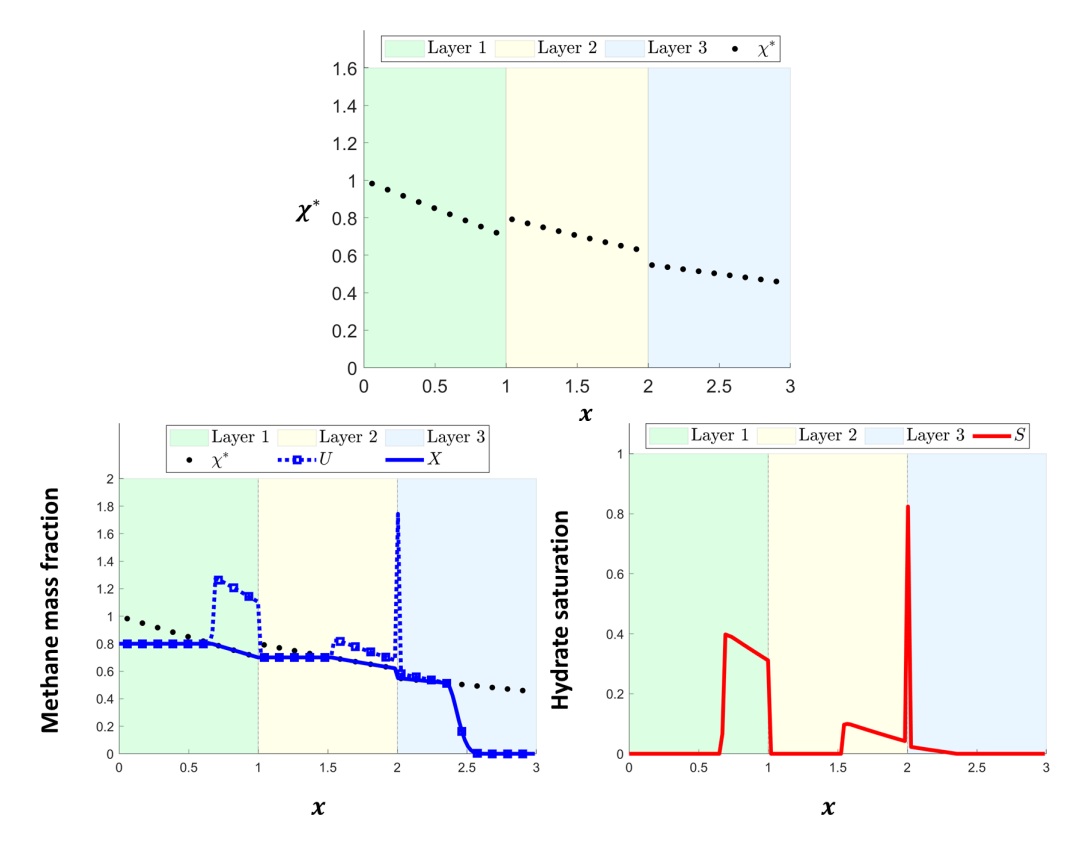


FIGURE 7. Transport in heterogeneous domain from Ex. 3 at T = 2.4. Top: layers of heterogeneous sediment with different maximum solubility curves χ^* at x = 1 and x = 2. Bottom: numerical solution. Of interest is behavior at the interfaces caused by the jumps of $\chi^*(x)$.

to vary due to the changing environmental conditions and specifically due to the warming of ocean temperature and the sea level rise as predicted in [40], with the rate of sea level rise is 0.003[m/y] and the rate of temperature rise at the seafloor of 0.01[K/y]. Then assume that the pressure (P), and temperature (T) at the seafloor vary linearly with respect to time t[y], with subscript ref and eq to denote the values at the seafloor and at the BHSZ, respectively.

$$P_{ref}(t) = \rho_l g D_{ref}(t), \quad D_{ref}(t) = D_{ref}(0) + 0.003t,$$

 $T_{ref}(t) = T_{ref}(0) + 0.01t,$

where $\rho_l \approx 1030 [\text{kg/m}^3]$ is the density of seawater, and $g = 9.8 [\text{m/s}^2]$. Over 150[y] we see the sea level rise by 0.45[m] and T_{ref} increase by 1.5[K]. Assume further that (P(x,t), T(x,t)) vary linearly in Ω

$$P(x,t) = P_{ref}(t) + G_H(d_{sf}(x) - D_{ref}(t)),$$

 $T(x,t) = T_{ref}(t) + G_T(d_{sf}(x) - D_{ref}(t)),$

where $d_{sf}(x)$ is the depth below the sea level. We then recompute the equilibrium conditions at BHSZ using the parametric model from [49] responding to the increase in T_{ref} , P_{ref} .

We apply these varying conditions to simulate the dissociation in a hydrate reservoir from the state obtained with simulation in Ex. 2 run until 100[ky]. We consider this state to be the initial state for this simulation at t = 0; see Fig. 10 with χ_0^* as shown. The changes in

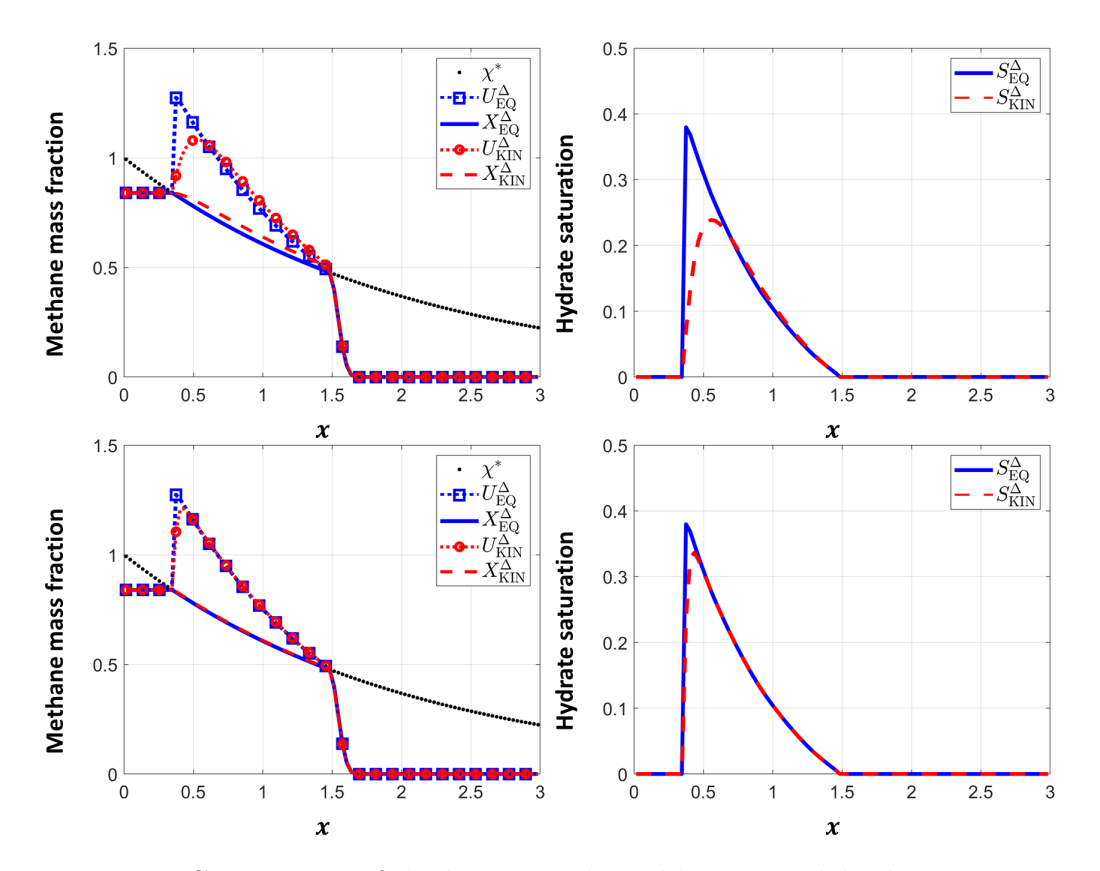


FIGURE 8. Comparison of the kinetic and equilibrium model solutions at T=1 with M=100, and $\nu=0.9$ for Ex. 4. Top: rate $k_3=10$. Bottom: rate $k_3=100$.

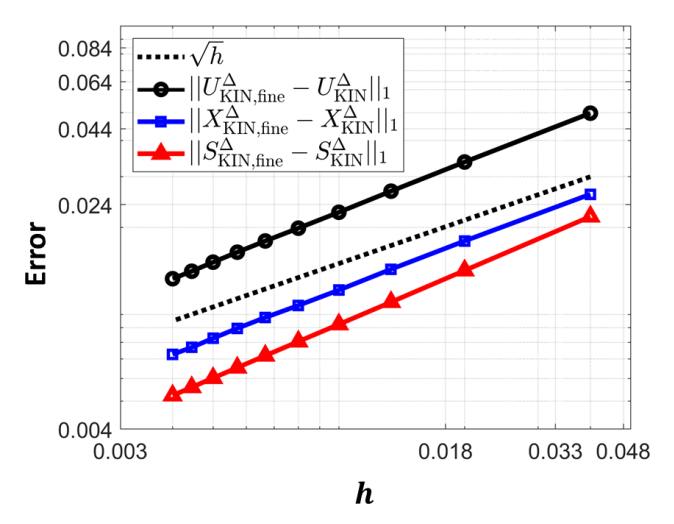


FIGURE 9. Convergence of the numerical solutions of Ex. 4 for $M = \{100, 200, \dots, 1000\}$ to the fine grid solution M = 50000 with $k_3 = 100$ at T = 1.

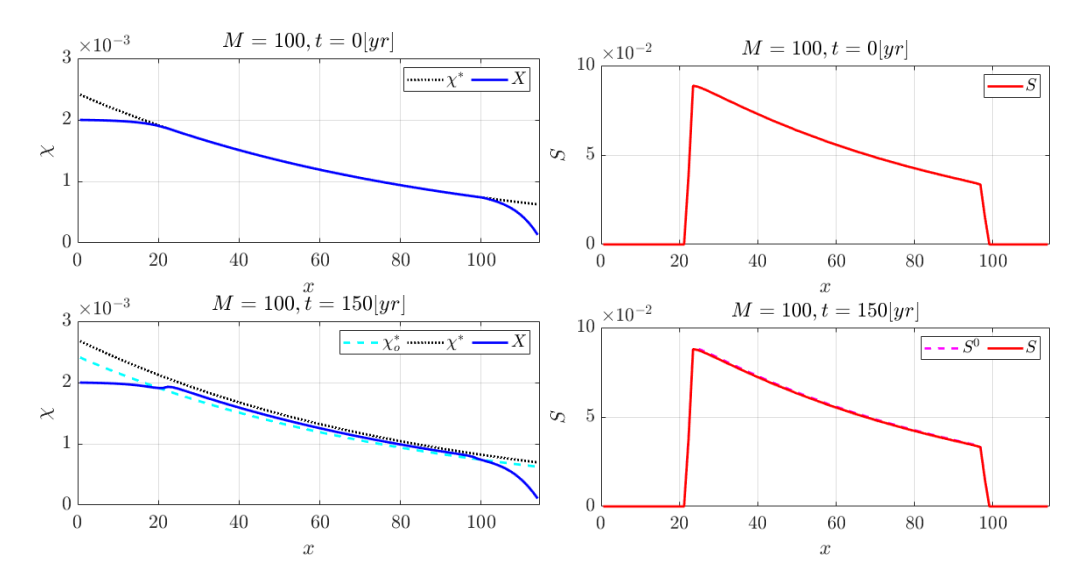


FIGURE 10. Top: initial condition $\chi(x,0)$ and S(x,0) from Sec. 8.3. Bottom: results of Ex. 5 with $k_3 = 0.01$. On both figures χ_0^* indicates the original $\chi^*|_{t=0}$.

P and T in time require we recompute $\chi^* = \chi^*(x,t)$ at the macro-time steps $T^m = m\Delta T$ as discussed in Sec. 5.2. We adopt other parameters as in Ex. 2 but use a fixed $\tau = 1[y]$ much smaller than that needed by CFL condition. We consider impact of $\Delta T = K\tau$, with K = 1, 10, 50, 150.

Example 5 (Hydrate dissociation due to warming waters). We start from the equilibrium state shown in Fig. 10. At every macro-time step $T^m = m\Delta T$, we recompute $\chi^*(x, T^m)$. Using the parameters as in Ex. 2 with $d_m = 3 \times 10^{-2} [\text{m}^2/\text{y}]$, we simulate hydrate dissociation using the (EQ) model at $t \in [0, 150]$ [y], and plot the solutions at the final $t^N = 150$ [y]. We compare the results to the numerical solutions generated by the equilibrium model (24) and the kinetic model (23), both amended to include diffusion, depending on different rates k_3 and the choice of ΔT .

At this time scale, dissociation proceeds slowly as shown by the decrease in the overall amount $||S||_1$ as well as the peak amount $||S||_{\infty}$; it is also interesting to test the magnitude S_2 of the last peak before the decrease to seafloor. For all simulations the peak $||S||_{\infty}$ is attained at x = 23.5[m], and the last saturation peak S_2 corresponds to x = 96.8[m].

We find the difference between taking macro-time steps with K = 1 up to K = 150 very small for both equilibrium and kinetic models, and the difference between kinetic model and equilibrium model indistinguishable when $k_3 = 100$. This rate is still about 100 times less than the rate used in [52, 64].

9. Conclusions and future work

In this paper we considered equilibrium and kinetic phase behavior for hydrate in twophase conditions typical in sediments above the bottom of Hydrate Stability Zone. Our objective was to study the stability of numerical models for transport coupled with phase transitions within IMPES-like time stepping for pressure and temperature. We provided

t[y]	K	$P_{ref}[MPa]$	$T_{ref}[K]$	$D_{ref}[{ m mbsl}]$	$P_{eq}[MPa]$	$T_{eq}[K]$	$D_{eq}[{ m mbsl}]$	$100 S _{\infty}$	$100S_{2}$	$ S _1$
0	_	21.6500	273.5500	2145.00	22.8849	294.6665	2268.49	8.8732	3.3524	4.3681
150	1	21.6545	275.0500	2145.45	22.7999	294.6364	2259.99	8.7212	3.2854	4.2848

TABLE 1. Simulation reference data and results generated by the equilibrium model (EQ) with K = 1 for Ex. 5.

		$k_3 = 0.01$			$k_3 = 1$			$k_3 = 100 \text{ and EQ}$		
t[y]	K	$100 S _{\infty}$	$100S_{2}$	$ S _{1}$	$100 S _{\infty}$	$100S_{2}$	$ S _{1}$	$100 S _{\infty}$	$100S_{2}$	$ S _{1}$
150	1	8.7946	3.3185	4.3295	8.7181	3.2844	4.2855	8.7212	3.2854	4.2848
150	10	8.7905	3.3168	4.3276	8.7168	3.2839	4.2848	8.7212	3.2854	4.2847
150	50	8.7736	3.3096	4.3196	8.7160	3.2836	4.2842	8.7212*	3.2854	4.2841
150	150	8.7381	3.2948	4.3044	8.7144	3.2831	4.2831	8.7213*	3.2855	4.2830

Table 2. Simulation results at t = 150[y] with kinetic model for Ex.5 with $\Delta t = K\tau$. (*) The results in the last macro-column differ are higher for the EQ model by one digit.

rigorous justification why the commonly used numerical scheme is stable and robust, and showed convergence with rate $O(\sqrt{h})$ consistent with that for monotone scheme and scalar conservation law in the presence of discontinuities. We also explained the presence of "spikes" of hydrate saturation similar to those observed in nature.

In addition, we investigated robustness of a variety of kinetic models in the two phase liquid-hydrate conditions. Such models are needed, e.g., during sudden rearrangement of external controls on thermodynamic equilibria. Since the kinetic model popular in literature dubbed (KIN1) and its linear variant called (KIN2) work only in saturated conditions, we developed another model (KIN3) which is robust across the unsaturated and saturated conditions and is equivalent to (KIN2) in saturated conditions. We combined this model (KIN3) with the transport model and were able to show its numerical stability.

The rigorous numerical analysis results we demonstrate are new; we are not aware of any other analysis of this type for hydrate models for either equilibrium and kinetic case.

More work is needed. In particular, extensions of the analysis for both the equilibrium and extensions of (KIN3) model for three phase conditions are needed; this is subject to our current work.

10. APPENDIX: AUXILIARY RESULTS

10.1. Proof of Proposition 1 on the stability of upwind scheme (26) for $u_t + f(x,t;u)_x = 0$ when f is smooth. We adapt the proof [32][Chapter 12] to the case when f = f(x,t;u); we require the boundedness of f_{xx} and f_{xu} uniformly in time. The proof is broken to thee parts. First we bound the difference $|\Delta U_j^n|$ between two adjacent values depending on $|\Delta U_j^{n-1}|$ and $|\Delta U_{j-1}^{n-1}|$. From this we conclude about $TV(U^n)$. Last we address $TV_T(U^{\Delta})$.

Local bounds on ΔU_i^n . We first subtract (26) at j-1 from that at j to get

$$\Delta U_j^n = \Delta U_j^{n-1} - \frac{\tau}{h} \left[\underbrace{F_j^{n-1} - F_{j-1}^{n-1}}_{(a)} \right] + \frac{\tau}{h} \left[\underbrace{F_{j-1}^{n-1} - F_{j-2}^{n-1}}_{(b)} \right],$$

where ΔU_j^{n*} denotes $U_j^{n*} - U_j^{n*-1}$ for n* = n and n-1. Since f is smooth, we can rewrite

$$\begin{array}{lcl} (a) & = & f(x_j,t^{n-1};U_j^{n-1}) - f(x_j,t^{n-1};U_{j-1}^{n-1}) + f(x_j,t^{n-1};U_{j-1}^{n-1}) - f(x_{j-1},t^{n-1};U_{j-1}^{n-1}) \\ & = & f_u(x_j,t^{n-1};\widetilde{U}_j^{n-1})\Delta U_j^n + f_x(\widetilde{x}_j,t^{n-1};U_{j-1}^{n-1})h \end{array}$$

where $\widetilde{U}_j^{n-1} \in (U_{j-1}^{n-1}, U_j^{n-1})$ and $\widetilde{x}_j \in (x_{j-1}, x_j)$, and similarly

$$(b) = f_u(x_{j-1}, t^{n-1}; \widetilde{U}_{j-1}^{n-1}) \Delta U_{j-1}^{n-1} + f_x(\widetilde{x}_{j-1}, t^{n-1}; U_{j-2}^{n-1}) h$$

where $\widetilde{U}_{j-1}^{n-1} \in (U_{j-2}^{n-1}, U_{j-1}^{n-1})$ and $\widetilde{x}_{j-1} \in (x_{j-2}, x_{j-1})$. After the substitution, we get

$$\Delta U_{j}^{n} = \left(1 - \frac{\tau}{h} f_{u}(x_{j}, t^{n-1}; \widetilde{U}_{j}^{n-1})\right) \Delta U_{j}^{n-1} + \frac{\tau}{h} f_{u}(x_{j-1}, t^{n-1}; \widetilde{U}_{j-1}^{n-1}) \Delta U_{j-1}^{n-1} - \tau \left[\underbrace{f_{x}(\widetilde{x}_{j}, t^{n-1}; U_{j-1}^{n-1}) - f_{x}(\widetilde{x}_{j-1}, t^{n-1}; U_{j-2}^{n-1})}_{(c)}\right].$$

Applying mean value theorem to f_x terms we rewrite (c) as

$$\begin{array}{lll} (c) & = & f_x(\widetilde{x}_j,t^{n-1};U_{j-1}^{n-1}) - f_x(\widetilde{x}_j,t^{n-1};U_{j-2}^{n-1}) + f_x(\widetilde{x}_j,t^{n-1};U_{j-2}^{n-1}) - f_x(\widetilde{x}_{j-1},t^{n-1};U_{J-2}^{n-1}), \\ & = & f_{xu}(\widetilde{x}_j,t^{n-1};\overline{U}_{j-1}^{n-1})\Delta U_{j-1}^{n-1} + f_{xx}(\overline{x}_j,t^{n-1};U_{j-2}^{n-1})(\widetilde{x}_j-\widetilde{x}_{j-1}), \end{array}$$

where $\overline{U}_{j-1}^{n-1} \in (U_{j-2}^{n-1}, U_{j-1}^{n-1})$ and $\overline{x}_j \in (\widetilde{x}_{j-1}, \widetilde{x}_j) \subseteq (x_{j-2}, x_j)$. Next we substitute (c) to get

$$\Delta U_j^n = \left(1 - \frac{\tau}{h} f_u(x_j, t^{n-1}; \widetilde{U}_j^{n-1})\right) \Delta U_j^{n-1} + \frac{\tau}{h} f_u(x_{j-1}, t^{n-1}; \widetilde{U}_{j-1}^{n-1}) \Delta U_{j-1}^{n-1}$$

$$- \tau \left[f_{xu}(\widetilde{x}_j, t^{n-1}; \overline{U}_{j-1}^{n-1}) \Delta U_{j-1}^{n-1} + f_{xx}(\overline{x}_j, t^{n-1}; U_{j-2}^{n-1})(\widetilde{x}_j - \widetilde{x}_{j-1})\right].$$

Next we take the absolute value of both sides and apply the triangle inequality. Since the CFL condition (28) holds, we get

$$\left| \Delta U_{j}^{n} \right| \leq \left(1 - \frac{\tau}{h} f_{u}(x_{j}, t^{n-1}; \widetilde{U}_{j}^{n-1}) \right) \left| \Delta U_{j}^{n-1} \right| + \frac{\tau}{h} f_{u}(x_{j-1}, t^{n-1}; \widetilde{U}_{j-1}^{n-1}) \left| \Delta U_{j-1}^{n-1} \right| + \tau \left| f_{xu}(\widetilde{x}_{j}, t^{n-1}; \overline{U}_{j-1}^{n-1}) \Delta U_{j-1}^{n-1} \right| + 2\tau h \left| f_{xx}(\overline{x}_{j}, t^{n-1}; U_{j-2}^{n-1}) \right|$$

Estimates on $TV(U^n)$. Now we take the sum over $j \in \mathbb{Z}$, keeping in mind the compact support of U^{Δ} , which reduces any sums over \mathbb{Z} to those over some finite set \mathbb{Z}^0 . We obtain

$$TV(U^{n}) \leq TV(U^{n-1}) - \frac{\tau}{h} \sum_{j \in \mathbb{Z}^{0}} f_{u}(x_{j}, t^{n-1}; \widetilde{U}_{j}^{n-1}) \left| \Delta U_{j-1}^{n-1} \right| + \frac{\tau}{h} \sum_{j \in \mathbb{Z}^{0}} f_{u}(x_{j-1}, t^{n-1}; \widetilde{U}_{j-1}^{n-1}) \left| \Delta U_{j-1}^{n-1} \right| + \tau \sum_{j \in \mathbb{Z}^{0}} \left| f_{xu}(\widetilde{x}_{j}, t^{n-1}; \overline{U}_{j-1}^{n-1}) \Delta U_{j-1}^{n-1} \right| + 2\tau \sum_{j \in \mathbb{Z}^{0}} \left| f_{xx}(\overline{x}_{j}, t^{n-1}; U_{j-2}^{n-1}) \right| h. \quad (46)$$

Re-indexing the third term on the right-hand-side of (46), the second and the third terms cancel each other. Using the definition of L_1 , we have

$$TV(U^n) \le TV(U^{n-1}) + \tau L_1 \sum_{j \in \mathbb{Z}^0} |\Delta U_{j-1}^{n-1}| + 2\tau L_1 \sum_{j \in \mathbb{Z}^0} h.$$

Since $|supp(f)| \leq \omega_S$, we have $\sum_{j \in \mathbb{Z}^0} h \leq \omega_S$. By re-indexing the second term, we get following:

$$TV(U^n) \le TV(U^{n-1})(1 + \tau L_1) + 2\tau L_1 \omega_S.$$

We repeat this inequality recursively to obtain

$$TV(U^n) \le TV(U^0)(1+\tau L_1)^n + 2\tau L_1 \omega_S \sum_{k=0}^{n-1} (1+\tau L_1)^k.$$

From Bernoulli inequality, $1 + \tau L_1 \leq e^{\tau L_1}$, we get $(1 + \tau L_1)^n \leq e^{n\tau L_1} \leq e^{TL_1}$ and we sum up the finite series to see that (30a) holds with $C_1(T) = TV(U^0)e^{TL_1} + 2\omega_S(e^{TL_1} - 1)$. **Variation in time.** We rewrite (26) as

$$U_j^n - U_j^{n-1} = -\frac{\tau}{h} \left[f_u(x_j, t^{n-1}; \widetilde{U}_j^{n-1}) \mid \Delta U_j^{n-1} \mid + f_x(\widetilde{x}_j, t^{n-1}; U_{j-1}^{n-1}) h \right],$$

where $\widetilde{U}_j^{n-1} \in (U_{j-1}^{n-1}, U_j^{n-1})$ and $\widetilde{x}_j \in (x_{j-1}, x_j)$. Take the absolute values of both sides and apply the triangle inequality to get

$$\left| U_j^n - U_j^{n-1} \right| \le \frac{\tau}{h} L_2 \left(\left| \Delta U_j^{n-1} \right| + h \right).$$

Next, we multiply both sides by h and sum over $j\in\mathbb{Z}^0$ to get

$$||U^n - U^{n-1}||_1 \le \tau L_2 \left[TV(U^{n-1}) + \omega_S \right].$$

Since $TV(U^n) \leq C_1(T)$ from (30a), now (30b) holds with $C_2(T) = L_2(C_1(T) + \omega_S)$. Finally, to get (30c), we combine (30a) and (30b), and obtain

$$TV_T(U^{\Delta}) \le C_3(T) = \sum_{n=0}^{T/\tau} \tau(C_1(T) + C_2(T)) = T(C_1(T) + C_2(T)).$$

10.2. Properties for the kinetic model. In this Section we provide details of fully implicit schemes for models batch reactor models (KINj), j = 1, 2, 3, respectively (18), (19), and (20). Our analysis motivates and supports the construction of the model (KIN3) which works across unsaturated and saturated conditions. Furthermore, our analysis helps to identify physically meaningful variables (χ, S) when working in non-isolated system, and to guide time stepping control. We define the discrete schemes in Sec. 10.2.1, and analyze their solvability and properties of solutions in Sec. 10.2.2. We illustrate the schemes and their properties in Sec. 10.2.3.

Let each model (KINj) have its own rate $k_j > 0$. We define $\overline{k_j} = \tau k_j$, and $\widetilde{k_j} = \frac{\overline{k_j}}{1 + \overline{k_j}}$. We denote by (X^{∞}, S^{∞}) the equilibrium values on graph E.

We consider a uniform time step $\tau > 0$, and $t^n = n\tau$, and we seek the approximations $X^n \approx \chi(t^n), S^n \approx S(t^n)$ in one step $[t^{n-1}, t^n)$, using the initial conditions X^{n-1}, S^{n-1} . Other variables including $\Psi^n \approx \psi(t^n)$, and quantities such as Q^n , are denoted analogously. The total methane content $U^n = X^n + (R - X^n)S^n$. The solutions corresponding to model

(KINj) are denoted with subscripts (KINj) e.g., we use notation X_{KINj}^n . When more compact notation is desired, and there is no need to indicate the time step, we use simpler notation, e.g. X_j . When no distinction between models is needed, we drop subscript j, and denote the new time step value sought $X = X_{\text{KINj}}^n$, while we set the previous time step values equal $\overline{X} = X_{\text{KINj}}^{n-1}$. With this notation, each scheme advances $(\overline{X}, \overline{S})$ to the new time step value (X, S).

10.2.1. Discrete schemes for batch kinetic models and their properties. The schemes are fully implicit: for (KIN2) and (KIN3) the solutions can be calculated with a closed formula, but (KIN1) requires an additional solvers. We prove various properties, and compare the models. Discrete scheme for (KIN1). Given $(\overline{X}, \overline{S}) = (X_{\text{KIN1}}^{n-1}, S_{\text{KIN1}}^{n-1})$, find (X, S).

$$(1-S)X - (1-\overline{S})\overline{X} = \overline{k_1}(\chi^* - X), \tag{47a}$$

$$RS - R\overline{S} = \overline{k_1}(X - \chi^*).$$
 (47b)

Solver for (47): the calculation of (X, S) from (47) is coupled and not explicit. To get a useful formula, we first calculate formally from (47b)

$$S = \frac{\overline{k_1}(X - \chi^*)}{R} + \overline{S}. \tag{48}$$

Then we substitute (48) in (47a), and rearrange to get a quadratic equation for X

$$X = \frac{\overline{k_1}}{R}(R - X)(\chi^* - X) + \overline{S}X + (1 - \overline{S})\overline{X}. \tag{49}$$

The solvability of (49) is addressed in Property (B) proven below; we also suggest a practical solver.

(KIN1) summary: Given $(\overline{X}, \overline{S}) = (X_{\text{KIN1}}^{n-1}, S_{\text{KIN1}}^{n-1})$: Solve (49) for X.

Calculate S from (48).

Set $(X_{KIN1}^n, S_{KIN1}^n) = (X, S)$.

Discrete scheme for (KIN2). Given $(\overline{X}, \overline{S}) = (X_{KIN2}^{n-1}, S_{KIN2}^{n-1})$, calculate $\overline{\Psi} = \overline{S}(R - \overline{X})$, and find (X, Ψ) for which

$$X - \overline{X} = \overline{k_2}(\chi^* - X), \tag{50a}$$

$$\Psi - \overline{\Psi} = \overline{k_2}(X - \chi^*). \tag{50b}$$

Solver for (50): since (50a) is linear, we rearrange to get

$$X = \widetilde{k}_2 \chi^* + (1 - \widetilde{k}_2) \overline{X}, \tag{51}$$

Substituting to (50b) we get

$$\Psi = \overline{\Psi} + \widetilde{k_2}(\overline{X} - \chi^*). \tag{52}$$

After some algebra, we obtain also an explicit formula

$$S = \frac{\overline{k_2}(\overline{X} - \chi^*) + (1 + \overline{k_2})(R - \overline{X})\overline{S}}{(R - \overline{X}) + \overline{k_2}(R - \chi^*)}.$$
 (53)

(KIN2) summary: Given $(\overline{X}, \overline{S}) = (X_{\text{KIN2}}^{n-1}, S_{\text{KIN2}}^{n-1})$: Calculate $\overline{\Psi} = \overline{S}(R - \overline{X})$.

Calculate X from (51), Ψ from (52), and S from (53).

Set $(X_{KIN2}^n, S_{KIN2}^n) = (X, S)$.

Discrete scheme for (KIN3). Given $(\overline{X}, \overline{S}) = (X_{KIN3}^{n-1}, S_{KIN3}^{n-1})$, calculate $\overline{\Psi} = \overline{S}(R - \overline{X})$, and find (X, Ψ, W) .

$$X - \overline{X} = \overline{k_3}(W - X), \tag{54a}$$

$$\Psi - \overline{\Psi} = \overline{k_3}(X - W), \tag{54b}$$

$$W \in w_*(\Psi). \tag{54c}$$

Solver for (54): At a first glance, the scheme is more complicated than (50). However, we can exploit various properties of monotone graphs to simplify. First we calculate formally

$$X = \widetilde{k_3}W + (1 - \widetilde{k_3})\overline{X}, \tag{55}$$

which we we substitute in (54b) and rearrange as

$$\Psi + \overline{k_3}W = \overline{\Psi} + \overline{k_3}(\widetilde{k_3}W + (1 - \widetilde{k_3})\overline{X}), \ W \in w_*(\Psi).$$
 (56)

After a few steps of algebra we get

$$\Psi + \widetilde{k_3}W = \overline{\Psi} + \widetilde{k_3}\overline{X}, \ W \in w_*(\Psi). \tag{57}$$

Now we use the resolvent $\mathcal{R}_{\widetilde{k_3}}^{w^*}(\cdot)$ of w^* as defined in (1) to solve (57) for $\Psi \in \text{domain}(w_*)$

$$\Psi = \mathcal{R}_{\widetilde{k_3}}^{w^*} \left(\overline{\Psi} + \widetilde{k_3} \overline{X} \right).$$

Since this resolvent function has a simple form $\mathcal{R}_{\widetilde{k_3}}^{w^*}(w) = (w - \widetilde{k_3}\chi^*)_+$, with a few more substitutions we get

$$\Psi = (\overline{\Psi} + \widetilde{k}_3(\overline{X} - \chi^*))_+, \tag{58}$$

an explicit formula giving Ψ in terms of $\overline{X}, \overline{\Psi}$. Once Ψ is known, we calculate the auxiliary variable W from (57) by back-substituting (58), and we have $W = \frac{\overline{\Psi} - \Psi}{\widetilde{k}_3} + \overline{X}$, thus $W = \chi^*$ if $\Psi \geq 0$, and $W = \overline{X} + \frac{\overline{\Psi}}{\widetilde{k}_3}$ otherwise. These calculations allow to calculate X explicitly

$$X = \widetilde{k_3}\chi^* + (1 - \widetilde{k_3})\overline{X}$$
, if $\Psi \ge 0$, and $X = \overline{X} + \overline{\Psi}$, otherwise. (59)

(KIN3) summary: Given $(\overline{X}, \overline{S}) = (X_{\text{KIN3}}^{n-1}, S_{\text{KIN3}}^{n-1})$:

Calculate $\overline{\Psi} = \overline{S}(R - \overline{X})$.

Calculate Ψ from (58).

Given Ψ , calculate X from (59).

Calculate auxiliary variables $W = \frac{\overline{\Psi} - \Psi}{\widetilde{k}_3}$, and $S = \frac{\Psi}{R - X}$.

Set $(X_{KIN3}^{n-1}, S_{KIN3}^{n-1}) = (X, S)$.

10.2.2. Properties of schemes (KIN1), (KIN2), and (KIN3). Suppose that

$$(\overline{X}, \overline{S}) \in D^0. \tag{60}$$

Also, denote $\overline{\Psi} = (R - \overline{X})\overline{S}$. Below we prove solvability of (47), (50), and (54) as well as analyze qualitative properties of their solutions which we arrange in a list (A-B-C-D-E). Since each of the schemes is a one-step scheme, it is sufficient to only consider the properties of one step solutions (X, S) depending on $(\overline{X}, \overline{S})$.

Property (A): mass conservation.

If the solutions to any scheme j = 1, 2, 3 exist, they satisfy $U^n = u(X^n, S^n) = U^0$ where u(X, S) is given by (5b). In other words, for each scheme, the solutions (X^n, S^n) stay on the curve $u(X^n, S^n) = U^0$, and we have

$$S_j = \frac{U^0 - X_j}{R - X_j} = \frac{\overline{X} + (R - \overline{X})\overline{S} - X_j}{R - X_j}.$$
(61)

The map $S_j = S_j(X_j)$ is smooth and invertible when $0 \le X_j < R$.

Proof. The first part follows immediately by adding the two equations defining each scheme for one step, and following for n > 0 inductively. Analysis of (61) is straightforward.

Property (B): solvability of schemes.

Schemes (KIN2), (KIN3) are uniquely solvable, and (KIN1) is solvable depending on data and if τ is small enough.

Proof. The solutions to schemes (KIN2) and (KIN3) can be calculated from explicit algebraic expressions depending on the data $(\overline{X}, \overline{S})$, thus the conclusion is immediate.

However, scheme (KIN1) (47) requires a solution to the quadratic equation (49) which we frame as p(X) = 0 with

$$p(X) = \frac{\overline{k_1}}{R}(R - X)(\chi^* - X) + \overline{S}X + (1 - \overline{S})\overline{X} - X.$$
 (62)

We see that $p(\cdot)$ in (62) is a quadratic polynomial, with $p(0) = \overline{k_1}\chi^* + (1-\overline{S})\overline{X}$, and $p(R) = \overline{S}R - R + (1-\overline{S})\overline{X}$. Also, $p'(X) = \frac{2\overline{k_1}}{R}(X - X_R) + \overline{S} - 1$ where $X_R = \frac{R + \chi^*}{2}$. Now consider the root of p(X) = 0. From (60) we have that p(0) > 0, and $p(R) = (1-\overline{S})(\overline{X} - R) < 0$. Since $p(\cdot)$ is continuous, we see that the root to p(X) = 0 exists in [0, R] and in fact is in [0, R). Since, in addition, $p(\cdot)$ is convex, with $p''(X) = \frac{2\overline{k_1}}{R} > 0$, we find that this root is unique in [0, R), and is given from the quadratic formula

$$X = \frac{R(1-\overline{S}) + \overline{k_1}(R+\chi^*) - \sqrt{(R(1-\overline{S}) + \overline{k_1}(R+\chi^*))^2 - 4\overline{k_1}R(\overline{k_1}\chi^* + \overline{X}(1-\overline{S}))}}{2\overline{k_1}}$$
(63)

On the other hand, the second root given by a modification of (63) always exists in (R, ∞) , but is unphysical.

Lemma 4. Consider (KIN1) scheme. Suppose (60) holds and consider the smaller root $X = X_1 \in [0, R)$ of (62). Then (i) $S_1 < 1$.

(ii) If $\overline{X} < \chi^*$, then $\overline{X} < X < \chi^*$. If $\chi^* < \overline{X}$, then $\chi^* < X < \overline{X}$. If $\overline{X} = \chi^*$, then $X = \overline{X}$, and $S = \overline{S}$.

(iii) If $(\overline{X}, \overline{S}) \in D^0_+$ then $S_1 \ge 0$ for any $\overline{k_1}$.

(iv) On the other hand, suppose $(\overline{X}, \overline{S}) \in D^0_-$. If $\overline{S} = 0$, then $S_1 < 0$. If $\overline{S} > 0$, then for large $\overline{k_1}$ it is possible that $S_1 \leq 0$.

Proof. To prove (i), we recall Property (A) and (61). Since u < R, we have $S_1 = \frac{U^0 - X_1}{R - X_1} < 1$. To prove (ii), assume $\overline{X} < \chi^*$. First we collect the terms of (62) with X on the left hand side of the equation. Then subtract $(1 - \overline{S})\chi^*$ on the both sides of the equation to get

$$(\chi^* - X) \left[(1 - \overline{S}) + \frac{\overline{k_1}}{R} (R - X) \right] = (1 - \overline{S}) (\chi^* - \overline{X}).$$

Since $\overline{S} < 1$, and X < R, the second term on the left hand side and the first term on the right hand side are positive. Thus (i) the sign of $\chi^* - X$ is the same as that of $\chi^* - \overline{X}$. Further, rearrange p(X) = 0 as in the proof of Property B to read

$$\frac{\overline{k_1}}{R}(R-X)(\chi^*-X) = (1-\overline{S})(X-\overline{X}).$$

Similarly as above we conclude that the sign of $X - \overline{X}$ is the same as that of $\chi^* - X$, which completes the proof of (ii).

To prove (iii), take some $(\overline{X}, \overline{S}) \in D^0_+$ so that $u(\overline{X}, \overline{S}) \geq \chi^*$. By property (ii), we can have $\overline{X} > X > \chi^*$, or $\overline{X} < X < \chi^*$. (We omit the trivial case $X = \overline{X}$). In the first case by (48) we have $S_1 = \frac{\overline{k_1}(X - \chi^*)}{R} + \overline{S} \geq \overline{S} \geq 0$. In the second case by property A, (X, S_1) is on the curve $u(X, S_1) = u(\overline{X}, \overline{S}) \geq \chi^*$ which is above the curve $u(X, S) = \chi^*$. Thus $S_1 \geq 0$. To prove (iv), take $(\overline{X}, \overline{S}) \in D^0_-$, so we must have $\chi < \chi^*$. With $\overline{S} = 0$ we get from

To prove (iv), take $(X, S) \in D_{-}^{0}$, so we must have $\chi < \chi^{*}$. With S = 0 we get from (48) that $S_{1} = \frac{\overline{k_{1}}(X - \chi^{*})}{R} < 0$. Even if $\overline{S} > 0$, it is possible to find $\overline{k_{1}}$ large enough so that $\overline{S} \leq \frac{\overline{k_{1}}(\chi^{*} - \chi)}{R}$. For illustration, the curve $u(X, S_{1}) = u(\overline{X}, \overline{S}) \leq \chi^{*}$ is in this case below the curve $u(X, S) = \chi^{*}$, thus $S_{1} \leq 0$.

Property C: the solutions to (KINj) stay physically meaningful: $(X_j, S_j) \in D^0$, under some conditions for j = 1, 2 and unconditionally for j = 3.

- (i) The solutions (X_j, S_j) satisfy $0 \le X_j < R$ and $S_j < 1$ for all j.
- (ii) In addition, $S_3 \ge 0$ unconditionally.
- (iii) Let j = 1, 2. If $(\overline{X}, \overline{S}) \in D_+^0$, then $S_j \geq 0$. If $(\overline{X}, \overline{S}) \in D_-^0$ and either $\overline{S} > 0$ with $\overline{k_j}$ small enough, then $S_j > 0$. However, if $(\overline{X}, \overline{S}) \in D_-^0$ and either $\overline{S} = 0$, or if $\overline{k_j}$ is large, then it is possible that $S_j < 0$.

Proof of property C. (i) For (KIN1) Property B shows (i) for the correct root selected by the solver. For (KIN2), (51) shows that X_2 is a convex combination of \overline{X} and χ^* , thus $0 \le X_2 < R$. For (KIN3), when $\overline{S} + \widetilde{k_3}(\overline{X} - \chi^*) \ge 0$, X_3 is a convex combination of \overline{X} and χ^* , and the same argument applies. Otherwise, $X_3 = \overline{X} + \overline{S}(R - \overline{X}) < R$, and $0 \le X_3 < R$. To prove $S_j < 1$, we see that $X_j < R$ and by Property A $u(X_j, S_j) = u(\overline{X}, \overline{S}) < R$, thus from (61) it follows that $S_j < 1$.

To show (ii) consider (KIN3) first. we have $\Psi_3 \geq 0$ from (58), thus $S_3 \geq 0$. For scheme (KIN1), we use Lemma 4. For scheme (KIN2), we recall (52). To check if $0 \leq \Psi_2 = \overline{\Psi} + \widetilde{k_2}(\overline{X} - \chi^*)$, we first consider $\overline{X} \geq \chi^*$ (which implies $(\overline{X}, \overline{S}) \in D_+^0$). This yields $\Psi_2 \geq \overline{\Psi} \geq 0$, thus $S_2 \geq 0$. With $\overline{X} < \chi^*$ however, we find that to guarantee $\psi \geq 0$, we must have $\widetilde{k_2} < \frac{\overline{\Psi}}{(\chi^* - \overline{X})}$. For these, we recall $\frac{\overline{\Psi}}{(\chi^* - \overline{X})} = \frac{u - \overline{X}}{(\chi^* - \overline{X})}$, and this quantity $\frac{u - \overline{X}}{(\chi^* - \overline{X})} \geq 1$ in D_+^0 ,

while we have that for any τ , $0 < \widetilde{k_2} < 1$. We conclude that (KIN2) can produce unphysical $S_2 \le 0$ only for $(\overline{X}, \overline{S}) \in D_-^0$. If $\overline{\Psi} = 0$, we always have $\Psi_2 < 0$ and $S_2 < 0$.

Property D: stability of each scheme in Q.

We have $|Q_j| < |\overline{Q}|$ for each scheme.

Proof of property D. We recall that $Q_j = k_j(X_j - \chi^*)$ for j = 1, 2, and $Q_3 = k_3(X_3 - W)$ for (KIN3). We consider the bounds for j = 1 and (KIN1) first. We want to show $|\chi^* - X_j| \le |\chi^* - \overline{X}|$. To this aim, we subtract χ^* from both sides of (49), rearrange, and add $-\overline{S}\chi^*$ to both sides, and rearrange again to get

$$\left(1 - \overline{S} + \frac{\overline{k_1}}{R}(R - X)\right)(\chi^* - X_1) = (1 - \overline{S})(\chi^* - \overline{X}).$$

Next we take absolute value of both sides while we multiply them by k_1 . Since $1 - \overline{S} > 0$ and $\frac{\overline{k_1}}{R}(R - X) > 0$ from property C, we get, as desired

$$|Q_1| < \frac{1 - \overline{S}}{1 - \overline{S} + \frac{\overline{k_1}}{P}(R - X)} |\overline{Q}_1| < |\overline{Q}_1|.$$

For (KIN2), we add $\chi^* - X_2$ to both sides of (50a) to get

$$\overline{Q} = (1 + \overline{k_2})Q_2.$$

By $1 + \overline{k_2} > 1$ it is easy to see $|Q_2| < |\overline{Q}|$.

For (KIN3), the proof $|\overline{Q}_3| < |Q_3|$ is a special homogeneous case of a more general proof. We first consider Yosida approximation $w_{\lambda} \approx w_*$, or some other regularization which maintains the monotonicity properties of the graph w_* . Given $(\overline{X}, \overline{\Psi})$ we seek the solution $(X_{\lambda}, \Psi_{\lambda})$ to the regularization of (54) with $Q_{\lambda} = X_{\lambda} - w_{\lambda}(\Psi_{\lambda})$, and $\overline{Q} = \overline{X} - w_{\lambda}(\overline{\Psi})$

$$X_{\lambda} - \overline{X} + \overline{k_3} Q_{\lambda} = 0, \tag{64a}$$

$$\Psi_{\lambda} - \overline{\Psi} - \overline{k_3} Q_{\lambda} = 0. \tag{64b}$$

Next we multiply (64b) by $w'_{\lambda}(\Psi')$ with some $\Psi' \in (\overline{\Psi}, \Psi_{\lambda})$ to get

$$w_{\lambda}(\Psi_{\lambda}) - w_{\lambda}(\overline{\Psi}) - \overline{k_3}w_{\lambda}(\Psi')Q_{\lambda} = 0. \tag{65}$$

Subtract (65) from (64a), and take absolute value to get

$$(1 + \overline{k_3}(1 + w_{\lambda}(\Psi')) | Q_{\lambda}| = |\overline{Q}|.$$

Since $1 + \overline{k_3}(1 + w_{\lambda}(\overline{\Psi})) > 1$, we get the inequality $|Q_{\lambda}| < \frac{1}{1 + \overline{k_3}} |\overline{Q}|$ as desired. Taking the limit as $\lambda \to 0$ gives the desired result.

Property (E): (conditional) equivalence of schemes.

(i) Let $k_2 = k_3$. The schemes (KIN2) and (KIN3) give the same numerical solutions $X_2 = X_3$ iff $(\overline{X}, \overline{S}) \in D^0_+$. (ii) Moreover, if

$$k_1 = \frac{R\overline{k_2}(1-\overline{S})}{(R-\overline{X}) + \widetilde{k_2}(R-\chi^*)},\tag{66}$$

then the one-step solution to (KIN2) coincides with that for (KIN1).

Proof. To prove (i), we want to check if $X_2 = X_3$ by setting the right hand sides of (51) and (55) equal to each other. This identity holds if $\chi^* = \min\left(\overline{X} + (1 - \widetilde{k})\overline{\Psi}, \chi^*\right)$, which is equivalent to

$$\overline{S} \ge \frac{\widetilde{k}(\chi^* - \overline{X})}{R - \overline{X}}.\tag{67}$$

Now, if $(\overline{X}, \overline{S}) \in D^0_+$, we have $U = \overline{U} \ge \chi^*$, which means $\overline{S} \ge \frac{\chi^* - \overline{X}}{R - \overline{X}} \ge \frac{\widetilde{k}(\chi^* - \overline{X})}{R - \overline{X}}$ for any k and τ . Conversely, for (67) to hold, we must have $U \ge \chi^*$ since \widetilde{k} can be made arbitrarily close to 1.

To prove (ii), we want to calculate k_2 in terms of k_1 and previous time step data $(\overline{X}, \overline{S})$. Of course this is, in principle, always possible; the difficulty is to actually find this expression explicitly. We are able to do this and to obtain (66). We explain the process below.

Recall from (61) that S_j is a well defined invertible function of $X_j \in [0, R)$. In addition, for each scheme j, clearly each (X_j, S_j) is a function of $(\overline{X}, \overline{S})$ and of k_j . If these were given explicitly, one could write, e.g., $S_1 = S_2$ and attempt to solve for the dependence of k_1 on k_2 explicitly. Alternatively, one could do the same starting with $X_1 = X_2$ to get k_1 in terms of k_2 . However, the solver for (KIN1) does not give either X_1 not S_1 explicitly depending on $k_1, \overline{X}, \overline{S}$, and these direct strategies fail.

Instead, another possibility arises: we calculate $k_1 = k_1(\overline{X}, \overline{S}; X_1)$, with $\frac{\partial k_1}{\partial X_1} \neq 0$, after some analysis. Next we assume $X_1 = X_2$ and substitute $X_2 = X_2(k_2, \overline{X}, \overline{S})$ from (51). With this, we get an expression with k_1 in terms of $(k_2, \overline{X}, \overline{S})$ which is luckily explicit.

To get $k_1 = k_1(\overline{X}, \overline{S}; X_1)$, we recall (48) which binds together the constants k_1, \overline{S} and variables X_1, S_1 . With (61) we eliminate S_1 , and get a relationship between $k_1, \overline{S}, \overline{X}$ and X_1 , and we solve for $\overline{k_1}$

$$\overline{k_1} = \frac{R(\overline{X} - X_1)(1 - \overline{S})}{(R - X_1)(X_1 - \chi^*)}.$$
(68)

Now we assume $X_1 = X_2$, recall (51) in which X_2 is given $X_2 = X_2(\overline{X}, \overline{S}, k_2)$ explicitly and substitute this expression into (68) to get

$$\overline{k_1} = \frac{R(\overline{X} - \widetilde{k}_2 \chi^* - (1 - \widetilde{k}_2) \overline{X})(1 - \overline{S})}{(R - \widetilde{k}_2 \chi^* - (1 - \widetilde{k}_2) \overline{X})(\widetilde{k}_2 \chi^* + (1 - \widetilde{k}_2) \overline{X} - \chi^*)} = \frac{R\overline{k_2}(1 - \overline{S})}{(R - \overline{X}) + \widetilde{k}_2(\overline{X} - \chi^*)},$$

which, upon some algebra, is equivalent to (66).

10.2.3. Illustration of (KIN1), (KIN2), (KIN3) in batch setting. We illustrate now the three kinetic models with some numerical experiments. Our goal is to emphasize the similarities as well as the differences between these models. We employ the fully implicit schemes presented in Sec. 10.2.1. In the examples we use data R = 2, $\chi^* = 1$, and $k_j = 1$ for all j = 1, 2, 3.

Example 6 (Saturated case). Suppose that $u^0 = 1.64 > \chi^*$, thus the equilibrium state is $(\chi^{\infty}, S^{\infty}) = (1, 0.64)$ on the E^+_* portion of the E graph, and this example falls in the saturated regime. We consider two cases (I) $(X^0, S^0) = (0.2, 0, 8)$ and (II) $(X^0, S^0) = (1.4, 0.4)$. Both are in saturated regime $(X^0, S^0) \in D^0_+$. We use $\tau = 1$.

Fig. 11 illustrates the properties of the schemes from Sec. 10.2.1. We notice first that the property (A) holds: the numerical solutions (X_j^n, S_j^n) given by (47), (50), and (54) live on

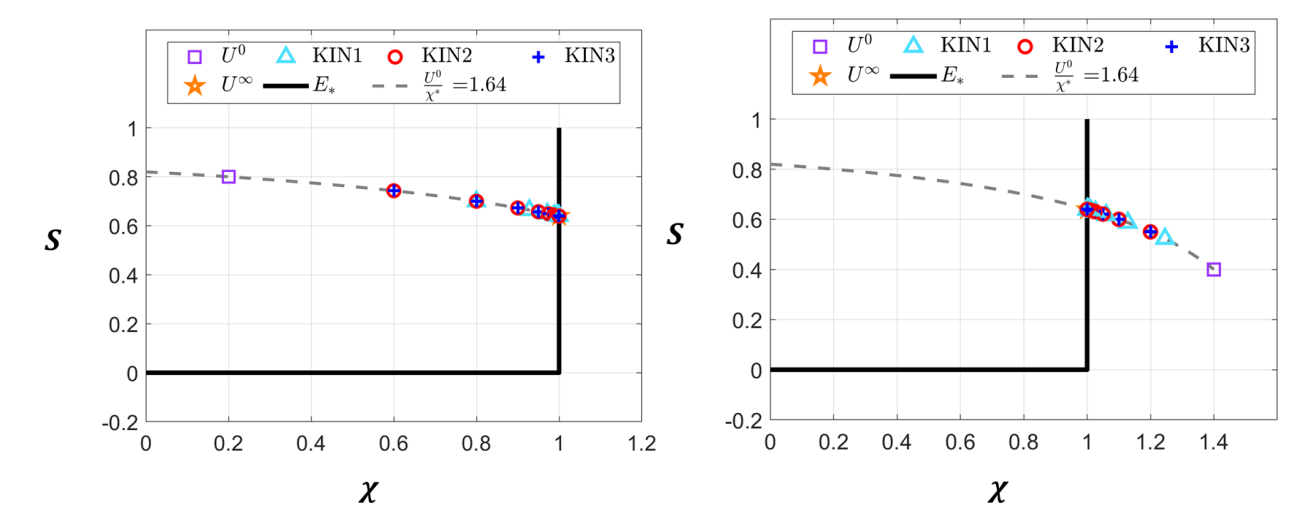


FIGURE 11. Simulation results for Ex. 6 illustrating schemes (KIN1), (KIN2), and (KIN3). Left: $(X^0, S^0) = (0.2, 0.8)$. Right: $(X^0, S^0) = (1.4, 0.4)$. The solutions to all schemes lie on the curve $u(X^n, S^n) = U^0$ and converge towards the equilibrium point (X^{∞}, S^{∞}) on the portion E_*^+ of the graph E. Solutions to (KIN2) and (KIN3) are indistinguishable.

the curve $U^n = u(X^n, S^n) = U^0 = u^0 = 1.64$, and as predicted by property (C), they stay in D^0 and are physical.

Second, according to property (D) the solutions to every scheme converge towards the equilibrium point (X^{∞}, S^{∞}) on the portion E_*^+ of the graph E_* , i.e., their distance Q from the equilibrium decreases. Third, as predicted by property (E), the solutions to (KIN2) and (KIN3) are indistinguishable, while the solutions to (KIN1) proceed at a rate different than that for (KIN2).

Example 7 (Unsaturated case). Suppose that $u^0 = 0.6$, thus the equilibrium state $(\chi^{\infty}, S^{\infty}) = (0.6, 0) \in E_*^-$. Now we choose $(X^0, S^0) = (0.25, 0.2) \in D_-^0$. We use large $\tau = 1$ or small $\tau = 0.5$.

Fig. 12 demonstrates the results of the three models depending on the time step. First, we see that all solutions live on curve $U^n = u(X^n, S^n) = u^0 = 0.6$. Second, for smaller τ we see that (KIN2) and (KIN3) coincide while in D^0_+ .

However, only the solutions $(X_{\text{KIN3}}^n, S_{\text{KIN3}}^n)$ to model (KIN3) converge to the equilibrium state on E_*^- , and stay physical for all time steps. In contrast, the solutions to (KIN1) and (KIN2), $(X_{\text{KIN1,2}}^n, S_{\text{KIN1,2}}^n)$ give unphysical solutions with negative saturations $S_j^n < 0$, and appear to converge to $X_j^\infty = \chi^*$ with $S_j^\infty = -0.4$ for which $Q_j = 0$. In fact, $(X_{\text{KIN1,2}}^n, S_{\text{KIN1,2}}^n)$ cross the graph E_*^- , as predicted above. In particular, for $\tau = 1$, we have $(X_{\text{KIN1}}^n, S_{\text{KIN1}}^n) \approx (0.7536, -0.1232)$ for n = 2 and $(X_{\text{KIN2}}^n, S_{\text{KIN2}}^n) \approx (0.625, -0.0182)$ for n = 1. For $\tau = 0.5$ this happens for larger n.

Example 8 (Equivalence of (KIN1) and (KIN2)). In this example we illustrate property E.ii. In each case we show that the solutions to (KIN1) are the same as those of (KIN2) when k_1 is appropriately chosen depending on k_2 and previous time step values. In turn, (KIN3) solutions are identical to (KIN2) in D_+^0 . See Fig. 13.

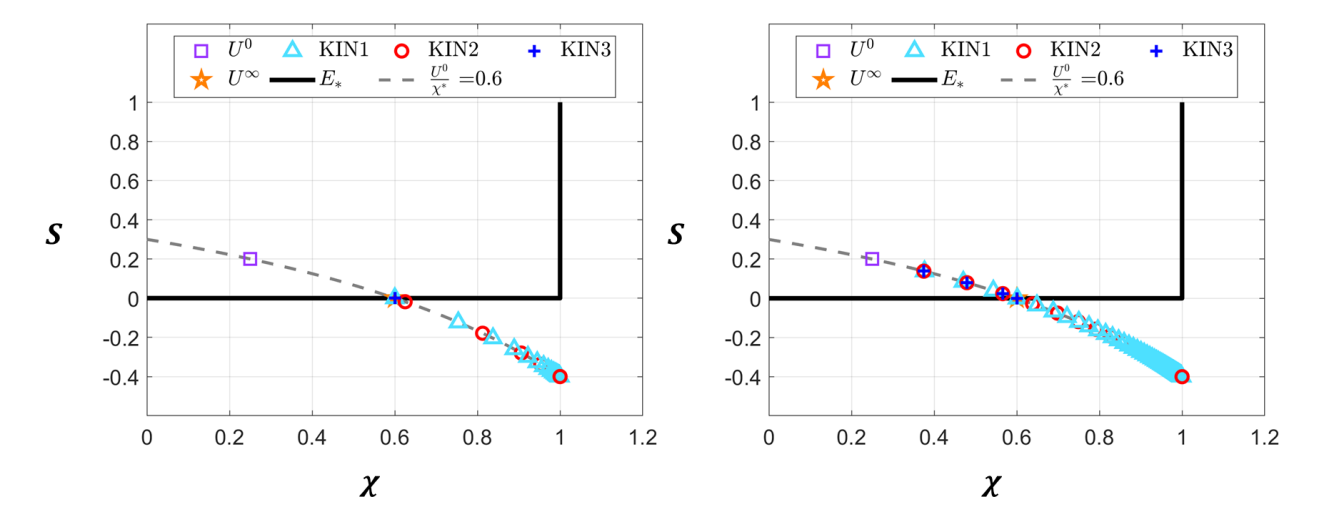


FIGURE 12. Simulation results of unsaturated case in Ex. 7 illustrating the behavior of kinetic models (KIN1), (KIN2), and (KIN3) with $(X^0, S^0) = (0.25, 0.2) \in E_*$. We use $\tau = 1$ (left) and $\tau = 0.2$ (right). The solutions to (KIN1) and (KIN2) become unphysical after a few time steps when the curve $u(\chi, S)$ crosses the E_* graph; the solutions to (KIN3) remain in D_-^0 . In addition, while in D^0 , the solutions to (KIN2) and (KIN3) are indistinguishable.

acknowledgements. The authors would like to thank the anonymous referees whose comments inspired additional results included in the paper as well as helped to improve the exposition. We also thank our colleague Ralph Showalter who made us aware of the paper [21]. We are grateful to our geoscience collaborators Marta Torres and Wei-Li Hong for motivating discussions. Choah Shin would like to thank Larry Martin and Joyce O'Neill for the generous support with the endowed College of Science at Oregon State fellowship 2019-20. Malgorzata Peszynska would like to thank the NSF DMS IRD plan 2019-21 funding which partially made this research possible. This material is based upon work supported by and while serving at the National Science Foundation. Any opinion, findings, and conclusions or recommendations expressed in this material are those of the authors and do not necessarily reflect the views of the National Science Foundation. This research was also partially supported by NSF DMS-1522734 "Phase transitions in porous media across multiple scales" and DMS-1912938 "Modeling with Constraints and Phase Transitions in Porous Media".

References

- [1] The National Methane Hydrates R&D Program Methane Hydrate Reservoir Simulator Code Comparison Study, http://www.netl.doe.gov/technologies/oil-gas/FutureSupply/MethaneHydrates/MH_CodeCompare/MH_CodeCompare.html.
- [2] The National Methane Hydrates R&D Program, http://www.netl.doe.gov/technologies/oil-gas/FutureSupply/MethaneHydrates/maincontent.htm.
- [3] T Almani, Kundan Kumar, A Dogru, G Singh, and MF Wheeler. Convergence analysis of multirate fixed-stress split iterative schemes for coupling flow with geomechanics. *Computer Methods in Applied Mechanics and Engineering*, 311:180–207, 2016.

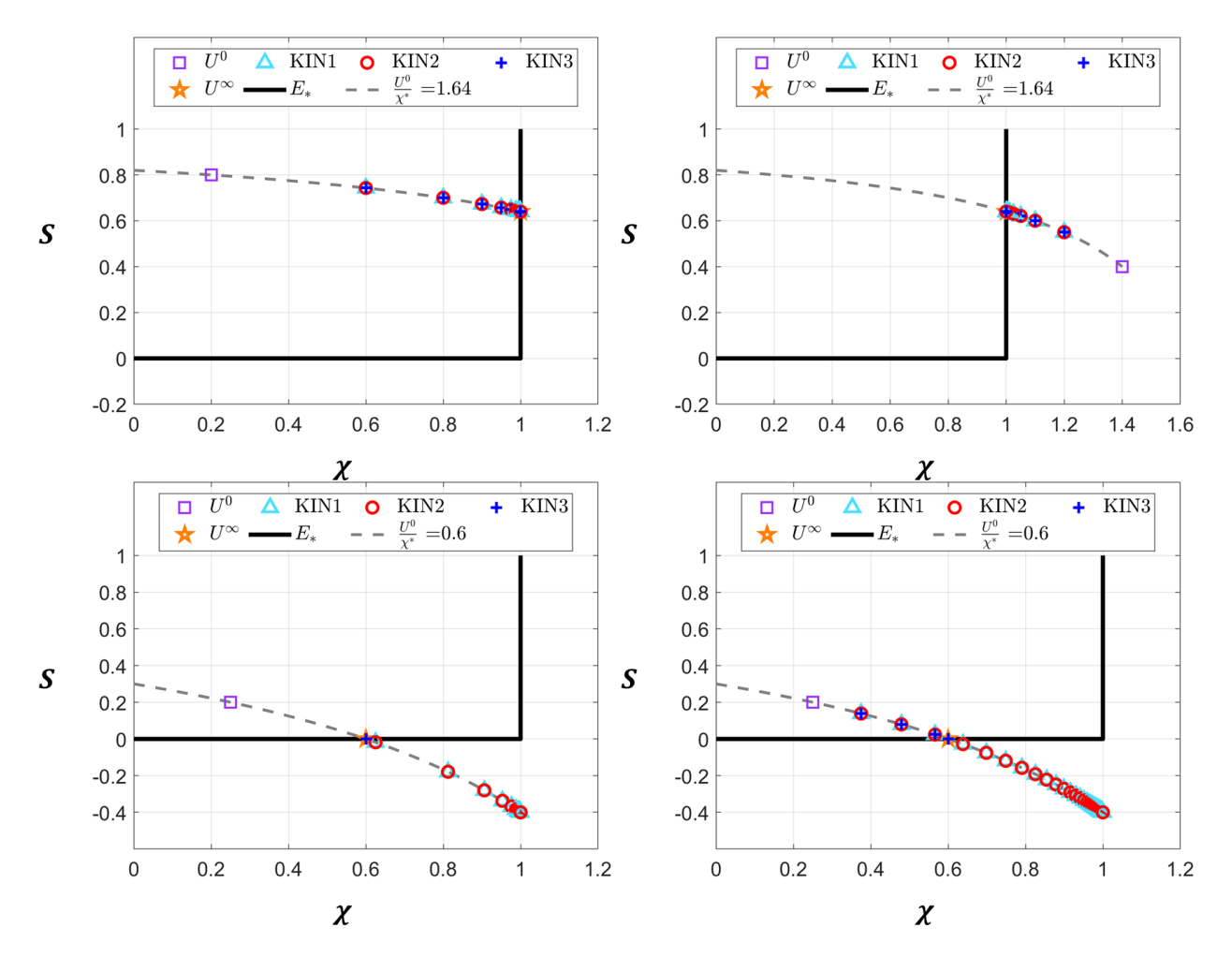


FIGURE 13. The numerical solutions generated by (KINj) for j=1,2,3 are the same with (66) for $(X^0,S^0)\in D^0_+$. For unsaturated cases, $(X^n_{\text{KIN1}},S^n_{\text{KIN1}})=(X^n_{\text{KIN2}},S^n_{\text{KIN2}})$.

- [4] Christian Berndt, Tomas Feseker, Tina Treude, Sebastian Krastel, Volker Liebetrau, H Niemann, Victoria J Bertics, Ines Dumke, Karolin Dunnbier, B Ferre, et al. Temporal constraints on hydrate-controlled methane seepage off Svalbard. *Science*, 343(6168):284–287, 2014.
- [5] H. Brézis. Opérateurs maximaux monotones et semi-groupes de contractions dans les espaces de Hilbert. North-Holland Publishing Co., Amsterdam, 1973. North-Holland Mathematics Studies, No. 5. Notas de Matemática (50).
- [6] Yuncheng Cao, Duofu Chen, and Lawrence M. Cathles. A kinetic model for the methane hydrate precipitated from venting gas at cold seep sites at hydrate ridge, Cascadia margin, Oregon. *Journal of Geophysical Research: Solid Earth*, 118(9):4669–4681, sep 2013.
- [7] Matthew A. Clarke and P. R. Bishnoi. Measuring and modelling the rate of decomposition of gas hydrates formed from mixtures of methane and ethane. *Chemical Engineering Science*, 56(16):4715–4724, 2001.
- [8] M. B. Clennell, M. Hovland, J.S. Booth, P. Henry, and W. Winters. Formation of natural gas hydrates in marine sediments: 1. conceptual model of gas hydrate growth conditioned by host sediment properties. *Journal of Geophysical Research*, 104:22,985–23,003, 1999.
- [9] H. Daigle and B. Dugan. Capillary controls on methane hydrate distribution and fracturing in advective systems. *Geochemistry, Geophysics, Geosystems*, 12(1), 2011.

- [10] M. K. Davie and B. A. Buffett. A numerical model for the formation of gas hydrate below the seafloor. Journal of Geophysical Research: Solid Earth, 106(B1):497–514, jan 2001.
- [11] M. K. Davie and B. A. Buffett. A steady state model for marine hydrate formation: Constraints on methane supply from pore water sulfate profiles. *Journal of Geophysical Research: Solid Earth*, 108(B10):n/a-n/a, oct 2003.
- [12] M. K. Davie, O. Y. Zatsepina, and B. A. Buffett. Methane solubility in marine hydrate environments. *Marine Geology*, 203(1-2):177–184, jan 2004.
- [13] G. R. Dickens. Rethinking the global carbon cycle with a large, dynamic and microbially mediated gas hydrate capacitor. *Earth Planet. Sci. Lett.*, 213:169–183, 2003.
- [14] P. Englezos, N. Kalogerakis, P. D. Dholabhai, and P. R. Bishnoi. Kinetics of formation of methane and ethane gas hydrates. *Chemical Engineering Science*, 42(11):2647–2658, 1987.
- [15] S. K. Garg, J. W. Pritchett, A. Katch, K. Baba, and T. Fijii. A mathematical model for the formation and dossociation of methane hydrates in the marine environment. *Journal of Geophysical Research*, 113:B08201, 2008.
- [16] Nathan L. Gibson, F. Patricia Medina, Malgorzata Peszynska, and Ralph E. Showalter. Evolution of phase transitions in methane hydrate. *Journal of Mathematical Analysis and Applications*, 409(2):816 – 833, 2014.
- [17] Shubhangi Gupta, Rainer Helmig, and Barbara Wohlmuth. Non-isothermal, multi-phase, multi-component flows through deformable methane hydrate reservoirs. *Computational Geosciences*, 19(5):1063–1088, sep 2015.
- [18] Shubhangi Gupta, Barbara Wohlmuth, and Rainer Helmig. Multi-rate time stepping schemes for hydro-geomechanical model for subsurface methane hydrate reservoirs. *Advances in Water Resources*, 91(C):78–87, may 2016.
- [19] P. Henry, M. Thomas, and M. B. Clennell. Formation of natural gas hydrates in marine sediments: 2. thermodynamic calculations of stability conditions in porous sediments. *Journal of Geophysical Research*, 104:23,005–23,022, 1999.
- [20] Wei-Li Hong and Malgorzata Peszynska. Geochemical aspects. In Daviel Broseta, Livio Ruffine, and Arnaud Desmedt, editors, Gas Hydrates 2: Geoscience Issues and Potential Industrial Applications, pages 219–241. Wiley, 2018. Numerical modeling of gas hydrate dynamics in nature marine sediments: Case studies from Hydrate Ridge, Cascadia Margin and Ulleung Basin.
- [21] Ulrich Hornung and R. E. Showalter. Elliptic-parabolic equations with hysteresis boundary conditions. SIAM Journal on Mathematical Analysis, 26(4):775, 1995.
- [22] S. J. Hunter, D. S. Goldobin, A. M. Haywood, A. Ridgwell, and J. G. Rees. Sensitivity of the global submarine hydrate inventory to scenarios of future climate change. *Earth and Planetary Science Letters*, 367:105–115, 2013.
- [23] M.R Islam. A new recovery technique for gas production from Alaskan gas hydrates. *Journal of Petroleum Science and Engineering*, 11(4):267–281, 1994.
- [24] K. H. KARLSEN and J. D. TOWERS. Convergence of the lax-friedrichs scheme and stability for conservation laws with a discontinuous space-time dependent flux. *Chinese Annals of Mathematics*, 25(03):287–318, 2004.
- [25] Kenneth Karlsen, Henrik Risebro, and John Towers. L1 stability for entropy solutions of nonlinear degenerate parabolic convection-diffusion equations with discontinuous coefficients. Skr. K. Nor. Vidensk. Selsk., pages 1–49, 01 2003.
- [26] H. C. Kim, P. R. Bishnoi, R. A. Heidemann, and S. S. H. Rizvi. Kinetics of methane hydrate decomposition. *Chemical Engineering Science*, 42(7):1645–1653, 1987.
- [27] Jisheng Kou and Shuyu Sun. A new treatment of capillarity to improve the stability of impes two-phase flow formulation. *Computers & fluids*, 39(10):1923–1931, 2010.
- [28] S. N. Kruzhkov. The Cauchy problem in the large for certain nonlinear first-order differential equations. Dok1. Akad. Nauk SSSR, 132:36–39, 1960.
- [29] N.N Kuznetsov. Accuracy of some approximate methods for computing the weak solutions of a first-order quasi-linear equation. *USSR Computational Mathematics and Mathematical Physics*, 16(6):105–119, 1976.
- [30] Antonio C. Lasaga. Kinetic Theory in the Earth Sciences, volume 402. Princeton university press, 2014.

- [31] Randall J. LeVeque. Numerical Methods for Conservation Laws. Lectures in Mathematics. ETH Zürich. Birkhäuser Basel: Imprint: Birkhäuser, Basel, second edition, edition, 1992.
- [32] Randall J. LeVeque. Finite Volume Methods for Hyperbolic Problems. Cambridge texts in applied mathematics. Cambridge University Press, Cambridge; New York, 2002.
- [33] Yanghui Li, Mingjun Yang, Jiafei Zhao, Haifeng Liang, Yongchen Song, and Xuke Ruan. Numerical simulation of methane production from hydrates induced by different depressurizing approaches. *Energies*, 5(2):438–458, feb 2012.
- [34] X. Liu and P. B. Flemings. Passing gas through the hydrate stability zone at southern hydrate ridge, offshore Oregon. *EPSL*, 241:211–226, 2006.
- [35] X. Liu and P. B. Flemings. Dynamic multiphase flow model of hydrate formation in marine sediments. Journal of Geophysical Research, 112:B03101, 2008.
- [36] Xiaoli Liu and Peter B. Flemings. Capillary effects on hydrate stability in marine sediments. *Journal of Geophysical Research: Solid Earth* (1978–2012), 116(B7), 2011.
- [37] Lin Longwei, Blake Temple, and Wang Jinghua. Suppression of oscillations in Godunovs method for a resonant non-strictly hyperbolic system. SIAM Journal on Numerical Analysis, 32(3):841–864, 1995.
- [38] Tatsuo Maekawa, Shiro Itoh, Susumu Sakata, Shun-Ichiro Igari, and Noboru Imai. Pressure and temperature conditions for methane hydrate dissociation in sodium chloride solutions. *Geochemical Journal*, 29(5):325–329, 1995.
- [39] A. Malinverno, M. Kastner, M.E. Torres, and U.G. Wortmann. Gas hydrate occurrence from pore water chlorinity and downhhole logs in a transect across the northern Cascadia margin (integrated ocean drilling program expediction 311. *Journal of Geophysical Research*, 113:B08103, 2008.
- [40] Héctor Marín-Moreno, Michela Giustiniani, Umberta Tinivella, and Elena Piñero. The challenges of quantifying the carbon stored in arctic marine gas hydrate. Marine and Petroleum Geology, 71:76–82, Mar 2016.
- [41] A Moncorgé, H.A Tchelepi, and P Jenny. Modified sequential fully implicit scheme for compositional flow simulation. *Journal of Computational Physics*, 337:98–115, 2017.
- [42] George J. Moridis, Timothy S. Collett, Scott R. Dallimore, Tohru Satoh, Steven Hancock, and Brian Weatherill. Numerical studies of gas production from several CH₄ hydrate zones at the Mallik site, Mackenzie Delta, Canada. Journal of Petroleum Science and Engineering, 43(3-4):219–238, 2004.
- [43] George J Moridis and E. Dendy Sloan. Gas production potential of disperse low-saturation hydrate accumulations in oceanic sediments. *Energy Conversion and Management*, 48(6):1834–1849, 2007.
- [44] J. Nimblett and C. Ruppel. Permeability evolution during the formation of gas hydrates in marine sediments. *Journal of Geophysical Research*, 108:B9, 2420, 2003.
- [45] M. Peszynska. Never Heard of Methane Hydrate? That Might be Good News. SIAM News, January 2018.
- [46] M. Peszynska, E. Jenkins, and M. F. Wheeler. Boundary conditions for fully implicit two-phase flow model. In Xiaobing Feng and Tim P. Schulze, editors, Recent Advances in Numerical Methods for Partial Differential Equations and Applications, volume 306 of Contemporary Mathematics Series, pages 85–106. American Mathematical Society, 2002.
- [47] M. Peszynska, Q. Lu, and M. F. Wheeler. Coupling different numerical algorithms for two phase fluid flow. In J. R. Whiteman, editor, *MAFELAP Proceedings of Mathematics of Finite Elements and Applications*, pages 205–214, Uxbridge, U.K., 1999. Brunel University.
- [48] M. Peszynska, R. Showalter, and J. Webster. Advection of methane in the hydrate zone: Model, analysis and examples. *Mathematical Methods in Applied Sciences*, 38:4613–4629, November 2015.
- [49] Malgorzata Peszynska, Wei-Li Hong, Marta E. Torres, and Ji-Hoon Kim. Methane Hydrate Formation in Ulleung Basin Under Conditions of Variable Salinity: Reduced Model and Experiments. Transport in Porous Media, 114:1–27, 2016.
- [50] Malgorzata Peszynska, Francis Patricia Medina, Wei-Li Hong, and Marta E Torres. Reduced numerical model for methane hydrate formation under conditions of variable salinity. time-stepping variants and sensitivity. *Computation*, 4(1):1, 2015.
- [51] Florin Adrian Radu, Jan Martin Nordbotten, Iuliu Sorin Pop, and Kundan Kumar. A robust linearization scheme for finite volume based discretizations for simulation of two-phase flow in porous media. Journal of Computational and Applied Mathematics, 289:134–141, 2015.

- [52] A. W. Rempel. A model for the diffusive growth of hydrate saturation anomalies in layered sediments. Journal of Geophysical Research, 116(B10), Oct 2011.
- [53] A. W. Rempel and B. A. Buffett. Formation and accumulation of gas hydrate in porous media. *Journal of Geophysical Research: Solid Earth*, 102(B5):10151–10164, may 1997.
- [54] Carolyn Ruppel. Tapping methane hydrates for unconventional natural gas. *Elements*, 3(3):193–199, 2007.
- [55] Florin Sabac. The optimal convergence rate of monotone finite difference methods for hyperbolic conservation laws. SIAM Journal on Numerical Analysis, 34(6):2306–2318, 1997.
- [56] R. E. Showalter. Monotone operators in Banach space and nonlinear partial differential equations, volume 49 of Mathematical Surveys and Monographs. American Mathematical Society, Providence, RI, 1997.
- [57] E. D. Sloan and C. A. Koh. Clathrate Hydrates of Natural Gases, volume 130. CRC Press, third edition, 2009.
- [58] Andrew J. Smith, Peter B. Flemings, Xiaoli Liu, and Kristopher Darnell. The evolution of methane vents that pierce the hydrate stability zone in the world's oceans. *Journal of Geophysical Research:* Solid Earth, 119(8):6337–6356, 2014.
- [59] Tao Tang and Zhen Huan Teng. The sharpness of Kuznetsov's $O(\sqrt{\Delta x})$ l^1 -error estimate for monotone difference schemes. *Mathematics of Computation*, 64(210):581–589, 1995.
- [60] C. E. Taylor, D. D. Link, and N. English. Methane hydrate research at NETL Research to make methane production from hydrates a reality. JPSE, 56:186–191, 2007.
- [61] Pavel Tishchenko, Christian Hensen, Klaus Wallmann, and Chi Shing Wong. Calculation of the stability and solubility of methane hydrate in seawater. *Chemical Geology*, 219(1-4):37–52, jun 2005.
- [62] M. E. Torres, K. Wallmann, A. M. Tréhu, G. Bohrmann, W. S. Borowski, and H. Tomaru. Gas hydrate growth, methane transport, and chloride enrichment at the southern summit of Hydrate Ridge, Cascadia margin off Oregon. Earth and Planetary Science Letters, 226(1-2):225 – 241, 2004.
- [63] John D. Towers. Convergence of a difference scheme for conservation laws with a discontinuous flux. SIAM Journal on Numerical Analysis, 38(2):681–698, 2000.
- [64] Brandon P. VanderBeek and Alan W. Rempel. On the importance of advective versus diffusive transport in controlling the distribution of methane hydrate in heterogeneous marine sediments. *Journal of Geophysical Research: Solid Earth*, 123(7):5394–5411, Jul 2018.
- [65] Klaus Wallmann, M. Riedel, W. Hong, H. Patton, A. Hubbard, T. Pape, C. Hsu, C. Schmidt, J. Johnson, M. Torres, K. Andreassen, C. Berndt, and G. Bohrmann. Gas hydrate dissociation off Svalbard induced by isostatic rebound rather than global warming. *Nat Commun*, 9(1):83–83, 2018.
- [66] Matthew R Walsh, Carolyn A Koh, E Dendy Sloan, Amadeu K Sum, and David T Wu. Microsecond simulations of spontaneous methane hydrate nucleation and growth. Science (New York, N.Y.), 326(5956):1095–1098, 2009.
- [67] M. F. Wheeler and M. Peszynska. Computational engineering and science methodologies for modeling and simulation of subsurface applications. Advances in Water Resources, 25(8-12):1147-1173, 2002.
- [68] M. D. White, T.J. Kneafsey, Y. Seol, W. F. Waite, S. Uchida, J.S. Lin, E. M. Myshakin, X. Gai, S. Gupta, M. T. Reagan, A. F. Queiruga, S. Kimoto, Baker. R. C., R. Boswell, J. Ciferno, T. Collett, J. Choi, S. Dai, M. de La Fuente, P. Fu, T. Fujii, C. G. Intihar, J. Jang, X. Ju, J. Kang, J. H. Kim, J. T. Kim, S. J. Kim, C. Koh, Y. Konno, K. Kumagai, J. Y. Lee, W. S. Lee, L. Lei, F. Liu, H. Luo, G. J. Moridis, J. Morris, M. Nole, S. Otsuki, M. Sanchez, S. Shang, C. Shin, H. S. Shin, K. Soga, X. Sun, S. Suzuki, N. Tenma, T. Xu, K. Yamamoto, Yoneda. J., C. M. Yonkofski, H. C. Yoon, K. You, Y. Yuan, L. Zerpa, and M. Zyrianova. An international code comparison study on coupled thermal, hydrologic and geomechanical processes of natural gas hydrate-bearing sediments. Marine and Petroleum Geology, 120:104566, oct 2020.
- [69] Joseph W. Wilder, George J. Moridis, Scott J. Wilson, Masanori Kurihara, Yoshihiro Masuda, Brian J. Anderson, Timothy S. Collett, Robert B. Hunter, Hideo Narita, Mehran Pooladi-Darvish, and Ray Boswell. An international effort to compare gas hydrate reservoir simulators. volume 28, pages 493–501, 2008.
- [70] W. Xu. Modeling dynamic marine gas hydrate systems. American Mineralogist, 89:1271–1279, 2004.

- [71] W. Xu and C. Ruppel. Predicting the occurrence, distribution, and evolution of methane hydrate in porous marine sediments. *Journal of Geophysical Research*, 104:5081–5095, 1999.
- [72] Catherine M.R Yonkofski, Jake A Horner, and Mark D White. Experimental and numerical investigation of hydrate-guest molecule exchange kinetics. *Journal of Natural Gas Science and Engineering*, 35:1480–1489, 2016.
- [73] Kehua You, Timothy J Kneafsey, Peter B Flemings, Peter Polito, and Steven L Bryant. Salinity-buffered methane hydrate formation and dissociation in gas-rich systems. *Journal of Geophysical Research: Solid Earth*, 120(2):643–661, 2015.
- [74] M.H Yousif, H.H Abass, M.S Selim, and E.D Sloan. Experimental and theoretical investigation of methane-gas-hydrate dissociation in porous media. SPE (Society of Petroleum Engineers) Reservoir Engineering; (United States), 6(1):69–76, 1991.
- [75] Youxue Zhang. Geochemical Kinetics. Princeton University Press, Princeton, N.J., 2008.